Experimental investigations on solid and metal-cored creep-resistant wires deposited under GMA and PTA-based wire arc additive manufacturing (WAAM)

Published Version:
Iqbal, H., Pardal, G., Suder, W., Ascari, A., Fortunato, A., Liverani, E., et al. (2024). Experimental investigations on solid and metal-cored creep-resistant wires deposited under GMA and PTA-based wire arc additive manufacturing (WAAM). INTERNATIONAL JOURNAL, ADVANCED MANUFACTURING TECHNOLOGY, 136(3-4), 1207-1229 [10.1007/s00170-024-14926-5].

Availability:
This version is available at: https://hdl.handle.net/11585/1002432 since: 2025-01-20

Published:
DOI: http://doi.org/10.1007/s00170-024-14926-5

Experimental investigations on solid and metal-cored creep-resistant wires deposited under GMA and PTA-based wire-arc additive manufacturing (WAAM)

Hambal Iqbal[a,b], Goncalo Pardal[b], Wojciech Suder[b], Alessandro Ascari[a], Alessandro Fortunato[a], Erica Liverani[a], Stewart Williams[b], Leonor Neto[c]

[a]Department of Industrial Engineering, University of Bologna, Viale del Risorgimento 2 Bologna, 40136, Italy
[b]Welding and Additive Manufacturing Centre, Cranfield University, College road Cranfield, MK43 0AL, United Kingdom
[c]Welding Alloys Group, Unit 1, The old Livery, Hildersham Rd, Cambridge CB21 6DD, United Kingdom

Corresponding author: Hambal Iqbal (hambal.iqbal2@unibo.it)

ABSTRACT

Wire arc additive manufacturing (WAAM), also known as Arc-DED, possesses great potential for efficient production using various materials and wire types. This study utilized gas metal arc (GMA), and plasma transferred arc (PTA) variants of WAAM to deposit 2.25Cr-1Mo steel employing a metal cored-wire (MCW) and a solid wire counterpart having the same chemical composition for the comparative study. Initially, bead-on-plate trials were conducted with both WAAM processes and different shielding gas combinations in GMA-WAAM using the cored-wire. The heat input versus deposition ratio was analysed to assess the heat input and the effects of shielding gases in GMA-WAAM. Arc behaviour was monitored with a process camera, and bead morphologies and dilutions were compared. Furthermore, test walls were deposited under the two WAAM processes and the shielding gas conditions, employing the cored and solid wire. Detailed microstructural study was conducted through optical microscopy and hardness tests were performed to determine the mechanical properties. Energy dispersive X-ray spectroscopy (EDS) was used to examine the elemental composition and potential segregation in walls deposited with cored and solid wires. Results indicated a lower heat input when using cored-wire and variable heat input due to shielding gases. A bainitic/martensitic microstructure was observed in test walls deposited with cored and solid wires with comparable microstructural features. The PTA process produced higher hardness than GMA, and solid wire exhibited slightly higher hardness than cored-wire. Selection of shielding gas also influenced the hardness. Finally, the EDS maps and elemental study revealed comparable results for both wires. The results show good performance and outcome for cored-wire.

Keywords: WAAM; Cored-wire; DED-arc; metal additive manufacturing; PTA

1. INTRODUCTION

Wire arc additive manufacturing (WAAM) is a direct energy deposition (DED) process [1] that is widely used for layer wise fabrication of larger structures, to reduce the lead time and material wastage. Now a days, WAAM is alternatively being called Arc-DED process. An Arc-DED system utilizes a heat source integrated with a wire feeder to feed the wire through a nozzle across the welding torch. The welding torch is precisely moved by a motion system, usually employing a robot or a CNC gantry. The wire feedstock is fed across an electric arc, melted and deposited on the substrate in a controlled manner. The deposition follows a designated path controlled by the motion system. The application of wire as feedstock makes it more economical than powder feedstock [2] while achieving a high deposition rate of up to 5-6 kg/h [3]. WAAM offers a range of process variants including the gas metal arc (GMA) [4], gas tungsten arc (GTA) [5] and plasma transferred arc (PTA) [6]. These process variants are mainly differentiated based on the heat source (electric arc or plasma) and how the wire feedstock is fed and whether we have a consumable or non-consumable electrode. GMA process employs a consumable wire electrode and establishes the electric arc between the wire and substrate, melting and depositing the wire thereby. Conversely, GTA and PTA use a non-consumable tungsten electrode to sustain the arc and plasma, respectively. Then the consumable wire is fed from an external wire feeder, melting across the arc or plasma and deposited on the substrate or previously deposited layer(s). Thus, the former is suitable for a wide range of materials with high deposition rates while the latter two WAAM variants are ideal for superior quality deposits.

WAAM has gained substantial consideration due to its high material deposition rate, low capital cost, and versatility in depositing a range of materials including steel [7,8], aluminum alloys [9-11], titanium alloys [12-14], and nickel alloys [15,16]. It finds the applications in various industries including aerospace [17], automotive [18], and construction [19].

Chromium-molybdenum (Cr-Mo) steel, informally referred to as chromoly steel, is a creep-resistant material used in applications where elevated cyclic temperatures and pressures are experienced. A widely used low-alloyed variant of Cr-Mo steel is 2.25Cr-1Mo. They are preferred in power generation and petrochemical industries [20] due to their inherent properties. J. Vora et al. [21] employed a 1.25Cr-0.5Mo cored wire steel and studied the mechanical and microstructural properties in GMA-WAAM process. A defect free and uniform multi-walled component was deposited, and authors suggested the use of 1.25Cr-0.5Mo cored-wire in the WAAM process for industrial applications. Another study [22] employed a regulated metal transfer deposition (RMD) process to control the metal transfer in the short-circuit mode for welding a 10 mm thick weld joint using a 2.25Cr-1Mo steel using cored-wire. The researchers used the RMD technique for the root pass, followed by GMA for joint fill-up, and subjected the weldments to post-weld heat treatment and subsequent mechanical and metallurgical characterization. The authors proposed welding mid to high thickness with required properties as well as with enhanced productivity realized by metal-cored-wires. Another study [23] followed a similar approach for welding a 2.25Cr-1Mo using the cored-wire with a step cooling heat treatment approach to further assess the material properties, followed by EDX analysis and DBTT.

Very few studies have reported the application of GMA-WAAM in general and PTA-WAAM in particular for depositing 2.25Cr-1Mo steel using metal cored-wire (MCW). Cored-wires are tubular wires that come in two varieties such as flux-cored or metal-cored wires [24]. Flux-cored wire contains arc stabilizers aimed at increasing the weld quality while metal-cored wire improves the current density and deposition rate [25]. The current flows mostly through the outer tubular section of cored-wire, increasing the current density compared to solid wires. Consequently, reducing the overall heat requirements and thereby producing a lower heat input. To achieve similar deposition features such as bead shape, aspect ratio, and deposition speed, using a metal-cored wire requires less electrical current compared to a solid wire [26]. This difference is particularly beneficial for WAAM. However, due to the high deposition rate, elevated temperature, and excessive energy input, residual stresses and distortions are encountered in additive manufacturing (AM) processes, posing significant challenges. Therefore, generally in WAAM processes, achieving favorable outcome requires careful parameter selection [27], irrespective of the wire type. As mentioned earlier, the significant aspect of cored-wire lies in the fact that they allow in adopting customized alloying elements [28] in the core of the tubular wire and ultimately tailoring the chemical composition [29,30]. Studies have also shown the application of cored-wires in the production of complex concentrated alloys (CCAs) [31] and high entropy alloys [32]. This characteristic further instigates the opportunities offered by metal-cored wires for alloys' development and depositing materials with customized properties using the WAAM process.

WAAM process utilizes shielding gas during the metal deposition to protect the molten metal from contamination. The environmental contaminants and specially oxygen may cause oxidation of sensitive alloying elements, possibly leading to slag inclusions. Moreover, shielding gas also influences the arc ignition, bead formation, arc stability, wetting, weld penetration, and spatter formation. Several studies have investigated the use of different shielding gases in the WAAM process [33-37]. However, a systematic approach to investigate the effects of shielding gases on the heat input is still lacking in the literature. Although the main idea is to investigate the cored vs solid wire for the two different WAAM processes. One with the consumable electrode where the wire is in the hottest zone of the arc and the other with the non-consumable electrode in which wire is fed separately to the arc formed between the non-consumable electrode and workpiece. However, as the gas plays a significant role in protecting the liquid metal from oxidation and most importantly influencing the arc column formation, droplet formation, metal transfer and cathode spot stability. Therefore, various shielding gases were investigated employing the GMA process.

Some studies [38-43] have shown the use of cored-wires in WAAM processes, however, there is still not enough research on melting the cored-wires and in particular comparing to solid wire for the same material type. Therefore, this work aims to fill the knowledge gap by depositing a 2.25Cr-1Mo cored-wire in GMA and PTA-based WAAM processes. The study also investigates the use of different shielding gases in the melting of cored-wire in GMA process. Hence, the underlying study discusses cored vs solid wires in different WAAM processes.

2. MATERIALS AND METHODS

2.1. Experimental description

In this study a creep-resistance metal-cored wire 2.25Cr-1Mo (E90C-B3H4) was used for bead-on-plate studies in the first part, followed by the deposition of thin walls. For comparison, a high strength low alloy steel solid wire (ER90S-B3) of similar chemical composition was used for test walls deposition. Both the solid-wire and cored-wire have a diameter of 1.2 mm whose chemical compositions are reported in Table 1. A mild steel plate of 300 mm × 200 mm × 12 mm was used as substrate which was cleaned with acetone before deposition and was clamped with jigs. The depositions were performed employing GMA and PTA variants of WAAM process. The experimental setup of GMA and PTA-based WAAM process setups are shown in Fig. 1(a) and Fig. 1(b), respectively.

Table 1 Chemical composition [wt%] of the cored (E90C-B3H4) and solid (ER90S-B3) wires

Wire	C	Mn	Si	Cr	Mo	Fe
ER90S-B3	0.07-0.12	0.4-0.7	0.4-0.7	2.3-2.7	0.9-1.2	Bal.
E90C-B3 H4	0.06	0.8	0.3	2.3	1.0	Bal.

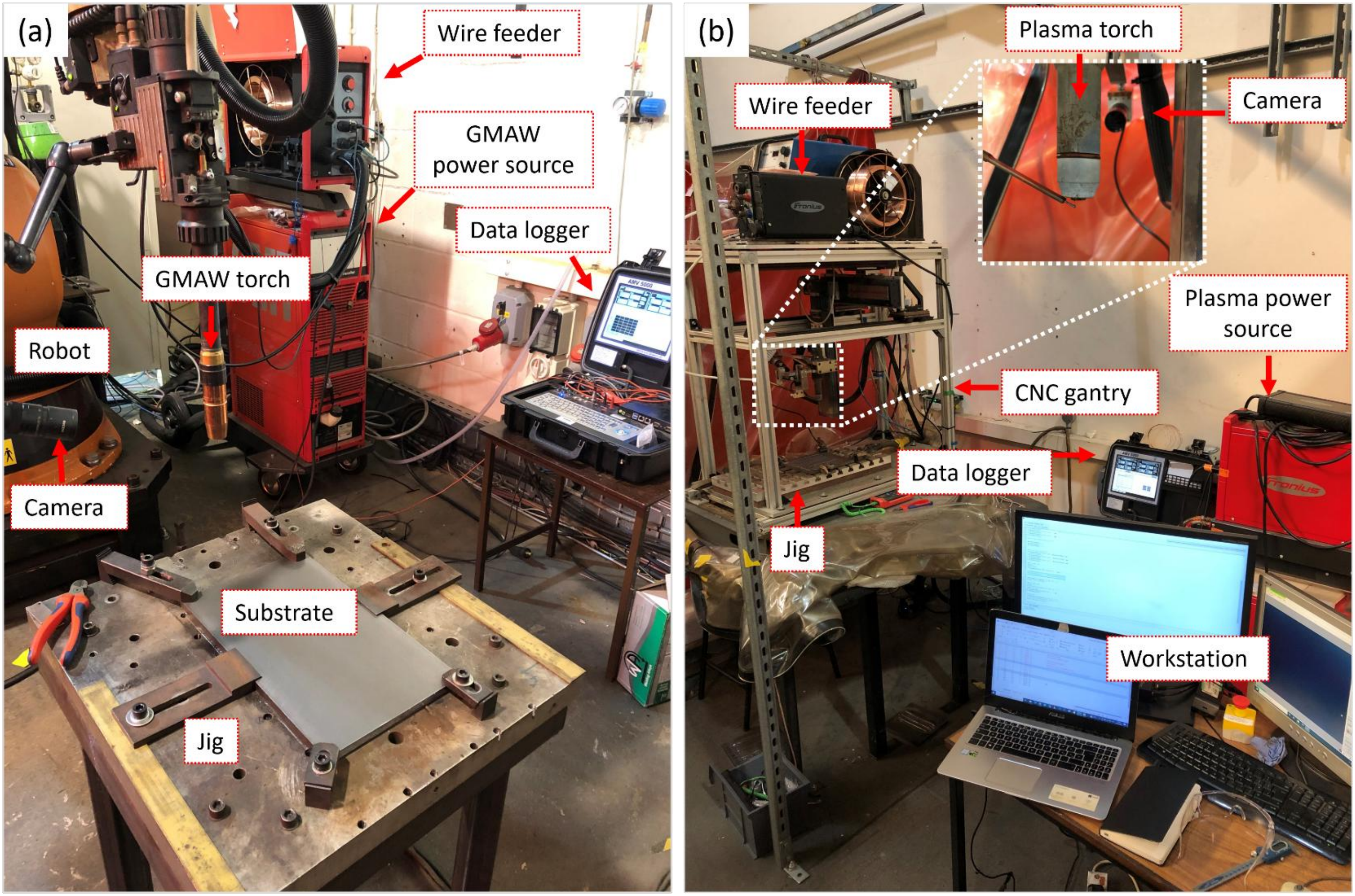

Fig. 1 Experimental setup: (a) GMA-WAAM, (b) PTA-WAAM

In GMA-WAAM, three shielding gases were used to investigate their influence on heat input, arc dynamics and bead morphology with bead-on-plate trials using only the cored-wire. Different combinations of wire feed speed (WFS) and travel speed (TS) were used. Following the deposition of bead-on-plate trials, five test walls were deposited with the three shielding gases using the cored and solid wires with most appropriate parameters. Table 2 represents the parameters and conditions for bead-on-plate trials and test walls. The 3 shielding gases combinations include pure argon, argon + 2.5% CO_2, and argon + 5% CO_2 + 2% O_2, at a flow rate of 15 l/min. For the sake of simplicity, they are referred to as pure argon, $ArCO_2$ and $ArCO_2O_2$, respectively, in the subsequent sections. Two test walls were deposited under $ArCO_2$ shielding using cord and solid wires. Similarly, two more walls were deposited using the cored and solid wires under the shielding of $ArCO_2O_2$, while another wall was deposited under pure argon shielding using the cored wire only. Fig. 2(a-c) shows the bead-on-plate trials in GMA-WAAM under different shielding gases: (a) pure argon, (b) $ArCO_2$, and (c) $ArCO_2O_2$. For each shielding gas combination, samples 1-4 were deposited with a TS of 0.6 m/min and WFS of 8, 10, 12, and 14 m/min were repeated, respectively. Similarly, the samples 5-8 were deposited using a TS of 0.8 m/min with the same WFS i.e. 8, 10, 12, and 14 m/min. The test walls were deposited with a WFS of 8 m/min and TS of 0.8 m/min, respectively under all shielding combinations and wire type. The contact-tip to work distance (CTWD) was maintained at 13 mm for bead-on-plate trials and test walls under all conditions. A Fronius power source was used in standard metal transfer mode i.e. short-circuit/spray mode and the welding torch was moved by a 6-axis Kuka robot.

In PTA-WAAM, bead-on-plate trials were performed with cored-wire, followed by deposition of two test walls using cored-wire and solid wire, respectively. A low power plasma source from Fronius was used with different combinations of current, travel speed (TS) and wire feed speed (WFS) for the bead-on-plate trials. Similarly, test walls were deposited with the most suitable process parameters. The parameters for bead-on-plate trials and test walls are given in Table 3. As shown in Fig. 2(d), bead-on-plate trials in PTA-WAAM were deposited by repeating the TS of 1.5 mm/s (0.09 m/min) and deposition current of 155A, for each WFS of 1, 1.2, 1.4, 1.6, and 1.8 m/min, respectively. This range of parameters was adopted to reach a similar range of WFS/TS for comparison between the two WAAM processes, discussed in section 3.1. To achieve a similar WFS/TS ratio, the operational limits of PTA-WAAM had reached, as can be seen by wavy beads in Fig. 2(d). Moreover, for the test walls, a suitable parameter set was used based on prior trials. This includes a deposition current of 185 A, TS of 3 mm/s and WFS of 1.4 m/min. However, in PTA-WAAM, the wall width tends to grow in the building direction due to heat accumulation and lower thermal conductivity when moving away from the substrate. This is due to the narrower path to conduct heat away compared to substrate. To avoid that, the initial current of 185 amperes used for the first two layers was gradually decreased by 5 amperes after every 1 – 2 layers until reaching to 125 amperes for layer number 19 and 20, respectively. This strategy proved to be very effective for consistent wall geometry and mitigated the overall heat input. Moreover, for plasma gas and arc shielding, pure argon was used at a flow rate of 0.8 and 8 liters per minute (l/min), respectively. The plasma torch, equipped with a non-consumable tungsten electrode was precisely moved by a CNC system. The distance between the nozzle and the substrate was maintained at 8 mm. The consumable wire electrodes were fed into the melt-pool with a vertex angle of 45°.

The test walls from both processes consisted of 20 layers each and 170 mm in length. The inter-layer temperature (ILT) was maintained below 150℃ during the deposition of walls in GMA and PTA processes. The ILT was maintained using a digital thermometer coupled with a k-type surface thermocouple. The deposition current and voltage were logged by connecting an arc monitor (AMV 4000) to the power sources in both processes. A process camera (Xiris XVC-1000) was used to record the process from the side of the melt-pool.

Table 2 Process parameters of GMA-WAAM for bead-on-plate deposits and test walls

Trial Type	WFS [m/min]	TS [m/min]	CTWD [mm]	Shielding gas	Wire type	Notes
Bead-on-plate	8, 10, 12, 14	0.6, 0.8	13	Pure Argon	Cored-wire	Each WFS repeated for each TS per gas
				$ArCO_2$	Cored-wire	
				$ArCO_2O_2$	Cored-wire	
Test Walls	8	0.8	13	Pure Argon	Cored-wire	1 wall deposited
				$ArCO_2$	Cored-wire	1 wall deposited
				$ArCO_2$	Solid wire	1 wall deposited
				$ArCO_2O_2$	Cored-wire	1 wall deposited
				$ArCO_2O_2$	Solid wire	1 wall deposited

Table 3 Process parameters of PTA-WAAM for bead-on-plate deposits and test walls

Trial Type	WFS [m/min]	TS [mm/s]	Current [A]	Shielding gas	Wire type	Notes
Bead-on-plate	1, 1.2, 1.4, 1.6, 1.8	1.5, 3, 4.5	155, 185, 215	Pure Argon	Cored-wire	Multiple trials for each parameter combination
Test Walls	1.4	3	185 - 125	Pure Argon	Cored-wire	1 wall deposited
				Pure Argon	Solid wire	1 wall deposited

2.2. Testing and characterization

Samples were obtained by cutting the deposited beads and walls from the middle section with a metallographic cutting machine (Discotom-60, Struers), resin mounted and polished up to 2500 grit papers, followed by the diamond suspension of 3 and 1 microns, respectively. To reveal the macro and microstructure, the mirror polished samples were etched with 2% Nital. Microstructural images were obtained with an optical microscope (Axiocam 208 color, ZEISS) with a magnification of 50 and 20 microns, respectively. Energy-dispersive X-ray spectroscopy (EDS) results were obtained from a TESCAN – VEGA3 equipped with an Oxford Instruments' EDS machine. An acquisition time of 60s at 500 magnification was used for EDS analysis which is better for smaller percentage of elements. For Vickers hardness an automatic hardness tester (Falcon500, Innovatest) was used with a load of 200g and an indentation time of 10s. Hardness indents were obtained starting below 0.5 mm from the top edge of the samples and continuing along the building direction until reaching the base metal.

3. RESULTS AND DISCUSSION

3.1. Arc stability and heat input in cored-wire

The bead-on-plate trials in GMA and PTA processes were conducted employing different wire feed speed (WFS), travel speed (TS) and current. Fig. 2(a – c) shows the deposited beads for GMA-WAAM under various shielding and PTA-WAAM under pure argon shielding. These parameters were selected to ensure the same deposition rate and were determined based on initial experiments. The bead-on-plate trials demonstrated in Fig. 2(d) show unsmooth and wavy beads representing the operational limit under the selected parameters. GMA-WAAM, employing a synergic operation, increases the deposition current and voltage with increasing WFS, ultimately increasing the heat input. The controlling parameters in this case become WFS and TS. In PTA-WAAM, unlike a synergic operation, the wire feeding is not coupled with power. That means, in PTA-WAAM, we can control the power input, WFS and TS separately, providing an extra degree of freedom compared to GMA-WAAM.

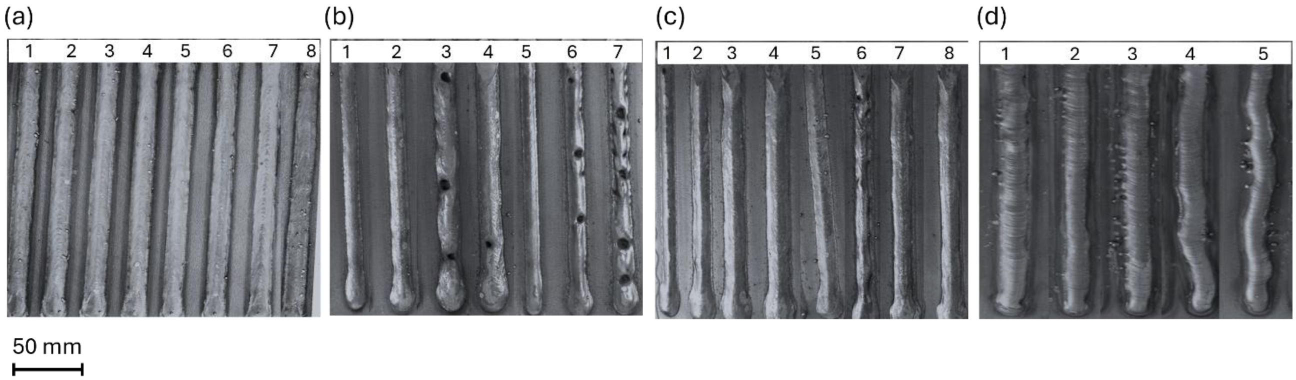

Fig. 2 Bead-on-plate trials in GMA-WAAM (a – c) under different shielding gases: (a) pure argon, (b) $ArCO_2$, and (c) $ArCO_2O_2$. Samples 1-4 were deposited with a TS of 0.6 m/min and WFS of 8, 10, 12, and 14 m/min, respectively. Samples 5-8 used a TS of 0.8 m/min with the same WFS. In trial (d), beads were deposited in PTA-WAAM at a TS of 1.5 mm/s (0.09 m/min) with a deposition current of 155A, using WFS of 1, 1.2, 1.4, 1.6, and 1.8 m/min, respectively.

Fig. 3 shows the arc stability in GMA-WAAM under various shielding gases. It was observed that arc fluctuations significantly reduced with the gases containing CO_2 and O_2. Hence, compared to pure argon, the argon mixture i.e. $ArCO_2$ gas improved the arc stability with less fluctuations of arc during the deposition. Similarly, the addition of O_2 further improved the arc stability compared to the other two gases when $ArCO_2O_2$ gas was used with a taller arc column. In this case, the arc appeared mostly straight with less oscillations and variations in shape and size. A better arc stability and spatter-free deposit was reported in the literature [32] using an argon-based shielding gas with 3% CO_2 + 1% O_2 compared to argon with 2% CO_2. This arc stability was attributed to stronger oxidizing property of O_2 leading to more uniform and thicker oxide layer on the bead, promoting higher electron emission, leading to better arc stability. Moreover, the improved arc stability can be attributed to lower activation energy for dissociation in CO_2 and O_2 gases compared to pure argon. A weaker activation energy for dissociation leads to higher thermal conductivity of gas and ultimately improving the arc stability. Similarly, the oxidizing property of oxygen promotes higher electron emission, further improving stability.

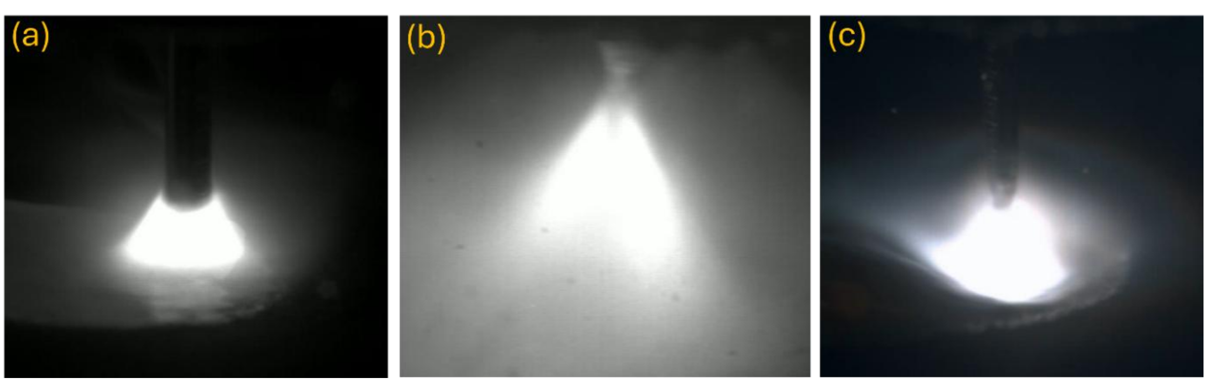

Fig. 3 Effects of shielding gases on arc stability under (a) $ArCO_2$, (b) $ArCO_2O_2$, and (c) Pure Argon

An important criterion for process comparison between PTA and GMA processes for WAAM deposition is the amount of material deposited per heat input. This could be possible by comparing the WFS versus heat input. However, one can notice that the WFS used in this study varies largely between the GMA and PTA processes due to the range of parameters offered by individual heat sources. Moreover, the GMA process follows a synergic operation from the controller of the heat source. Consequently, any increase of WFS proportionally increases the current and voltage. However, the PTA does not follow a synergic operation, and requires the adjustment of these process parameters individually. Therefore, a comparison solely based on WFS could not be possible. Nonetheless, another important factor in the WAAM process is the deposition ratio (WFS/TS), which is an important factor for material deposition rate. This indicates how much material in terms of wire is being deposited relative to the deposition speed, hence, effecting the buildup rate of the deposited structure. Fig. 4 shows such results for both WAAM processes. This also shows the influence of shielding gases i.e. $ArCO_2$ and $ArCO_2O_2$ and pure argon in GMA-WAAM. The heat input (H.I) was calculated for WAAM processes using the Eq. 1.

$$\text{H.I} \;=\; \frac{Current\;[A] \times Voltage\;[V]}{Travel\;speed\;[mm/s]} \times \eta\;[J/mm] \tag{1}$$

The η represents the energy efficiency of WAAM process. For consumable electrode GMA-WAAM and non-consumable electrode PTA-WAAM processes. Various ranges of efficiencies have been reported, however, 85% and 70% are commonly used for GMA and PTA processes, respectively [44,45]. Fig. 4 explicitly indicates that PTA-WAAM has generated a higher heat input for the same deposition ratio compared to GMA-WAAM process. Noticeably, In GMA-WAAM, the heat input also varies depending on the shielding gas used. For instance, addition of oxygen makes the process slightly colder for the same deposition ratio. Another study [46] revealed a lower heat input for pure argon compared to CO_2 gas, suggesting an increased ionization potential, leading to a hotter arc. As mentioned above, in GMA process the synergic waveform increases the deposition current and voltage when the wire feed speed is increased for a fixed travel speed. Consequently, raising the heat input. The rising trend of GMA-WAAM in the graph shows this behavior. However, as the PTA-WAAM is fully independent process (not synergic), therefore, the deposition current and voltage do not increase with increasing wire feed speed for a fixed travel speed. Any increase in wire feed speed would slightly decrease the heat input since more energy is used to melt the increasing volume of wire. Hence, it is safe to conclude that under the same process parameters, pure argon led to the lowest heat input where $ArCO_2$ produced the highest heat input and $ArCO_2O_2$ exhibited an intermediate heat input between these two gases in GMA-WAAM process. From the process point of view, considering the same deposition ratio, PTA-WAAM exhibited a much higher heat input compared to GMA process.

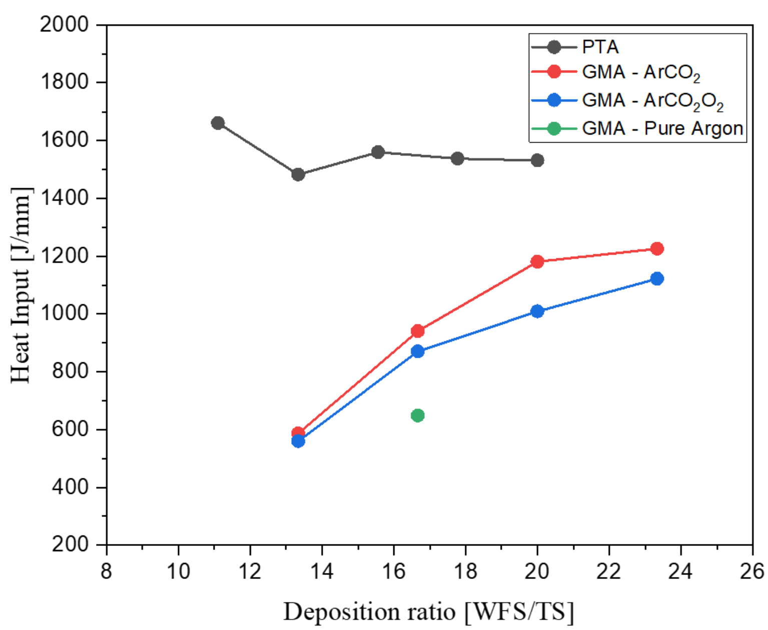

Fig. 4 Heat input vs deposition ratio in PTA-WAAM under pure argon and GMA-WAAM under various shielding gases

Fig. 5(a) represents the bead cross-sections, indicating the bead morphologies including the fusion area, remelt area and showing the heat affect zone (HAZ) for GMA and PTA processes, deposited with the cored-wire. On the other hand, Fig. 5(b) summarizes their corresponding values. The parameters used for these deposits were selected after several trials based on visual arc stability and general bead appearances and are the same parameters used for test walls as seen earlier in Table 2 and Table 3, respectively. With the same parameters, different shielding gases significantly affect the bead morphology, metal transfer mode, and bead penetration. Similarly, higher CO_2 and O_2 concentrations in pure argon gas stabilize the arc by increasing the metal vapor (i.e. more ionized particles) because of higher ionization potential and reduced surface tension, respectively [32]. The literature [34] revealed favorable layer formation when added oxygen in pure argon, however, the layer oxidation was increased which may not be favorable for part building of some materials. Comparing the shielding gases for bead-on-plate deposits in GMA-WAAM, one should notice distinct bead morphologies with characteristic features. The fusion area represents the deposited material above the substrate while the remelt area shows the part of the substrate that undergone remelting during the deposition. The HAZ represents the area where remelting did not occur, rather, it experienced a significant thermal history. Moreover, a larger remelt area shows that more energy was transferred to the substrate. A lower penetration, and a corresponding lower dilution is desirable in additive manufacturing since severe remelting of the previously deposited layers may lead to microstructural changes due to the thermal history. Hence, resulting in anisotropy of material properties.

Bead formation under pure argon shielding resulted in a narrow remelting zone, covering a smaller area at the edges, which led to the lowest dilution. However, it produced the highest HAZ in GMA-WAAM compared to other shielding gases. Under the shielding of $ArCO_2O_2$, an equal fusion area and a smaller HAZ were obtained, but a larger remelt area was observed compared to pure argon. Similarly, the bead deposited under $ArCO_2$ shielding resulted in a remelt area almost equal to that of pure argon in terms of surface area. However, the fusion area and HAZ were smaller compared to pure argon and $ArCO_2O_2$. When comparing the bead morphologies, the reinforcement height and width were consistent across all beads.

In contrast, PTA produced an oval-shaped bead, unlike the convex-shaped remelting area seen in GMA. PTA also resulted in higher penetration at the edges, covering a larger remelting area and leading to higher dilution. Moreover, it also produced the highest HAZ compared to those obtained in GMA. This could be attributed to the very high heat input of PTA compared to GMA.

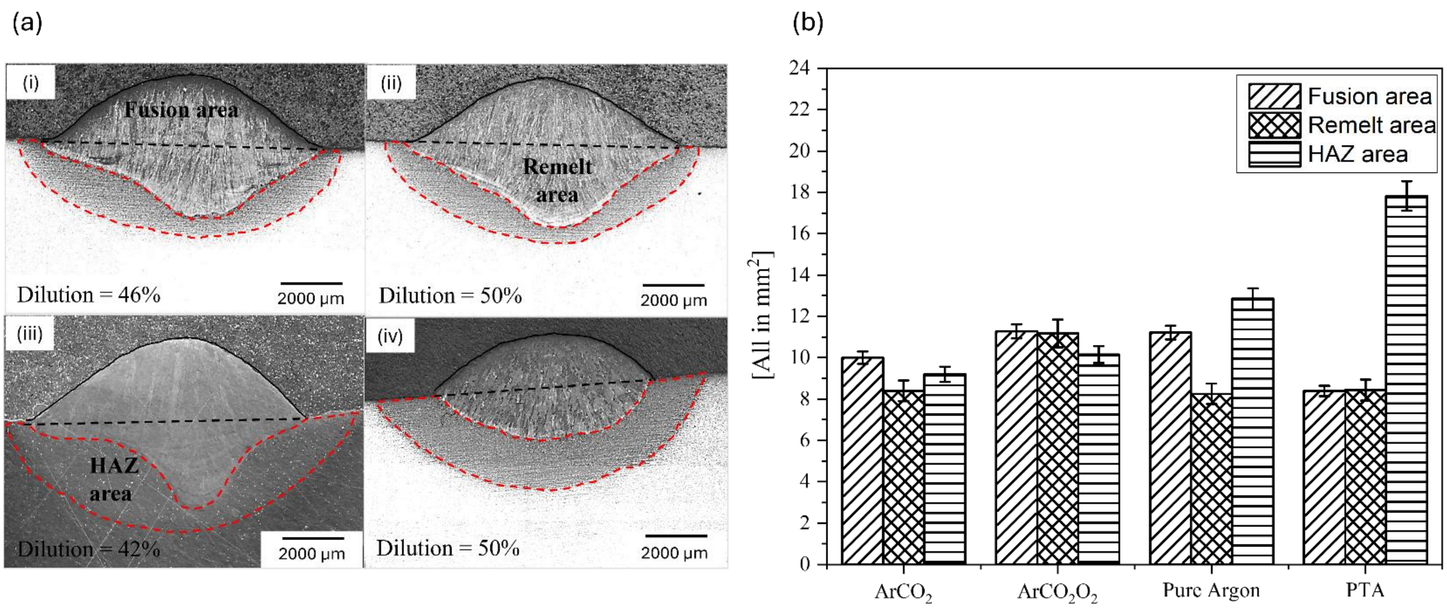

Fig. 5 (a) Bead cross-sections under the shielding of: (i) $ArCO_2$, (ii) $ArCO_2O_2$, and (iii) Pure Argon shielding in GMA-WAAM and (iv) PTA-WAAM process, (b) with their corresponding bead geometric features

Apart from the arc stability analysis, Fig. 6 illustrates in detail the arc dynamics, metal transfer, and spatters at different time instants under the same processing parameters for various shielding gases in GMA-WAAM and under pure argon shielding in PTA-WAAM. For GMA, the arc shape and size under $ArCO_2$ and pure argon shielding does not vary significantly in appearance, except that a slightly larger arc column is generated when using $ArCO_2$. On the other hand, $ArCO_2O_2$ formed a smaller and more stable arc around the tip of the wire in conical shape, producing a streamline metal transfer on the melt-pool. Small spatters appeared under all shielding conditions in GMA-WAAM, however, $ArCO_2O_2$ showed comparatively less spatter. Furthermore, PTA represented a more focused arc where the external wire electrode is fed and melted across the pure argon in a streamline metal transfer mode. The PTA process intermittently generated some spherical spatters thrown away from the melt-pool. The occurrence of spatters in PTA is less frequent than GMA, however, they are larger in size.

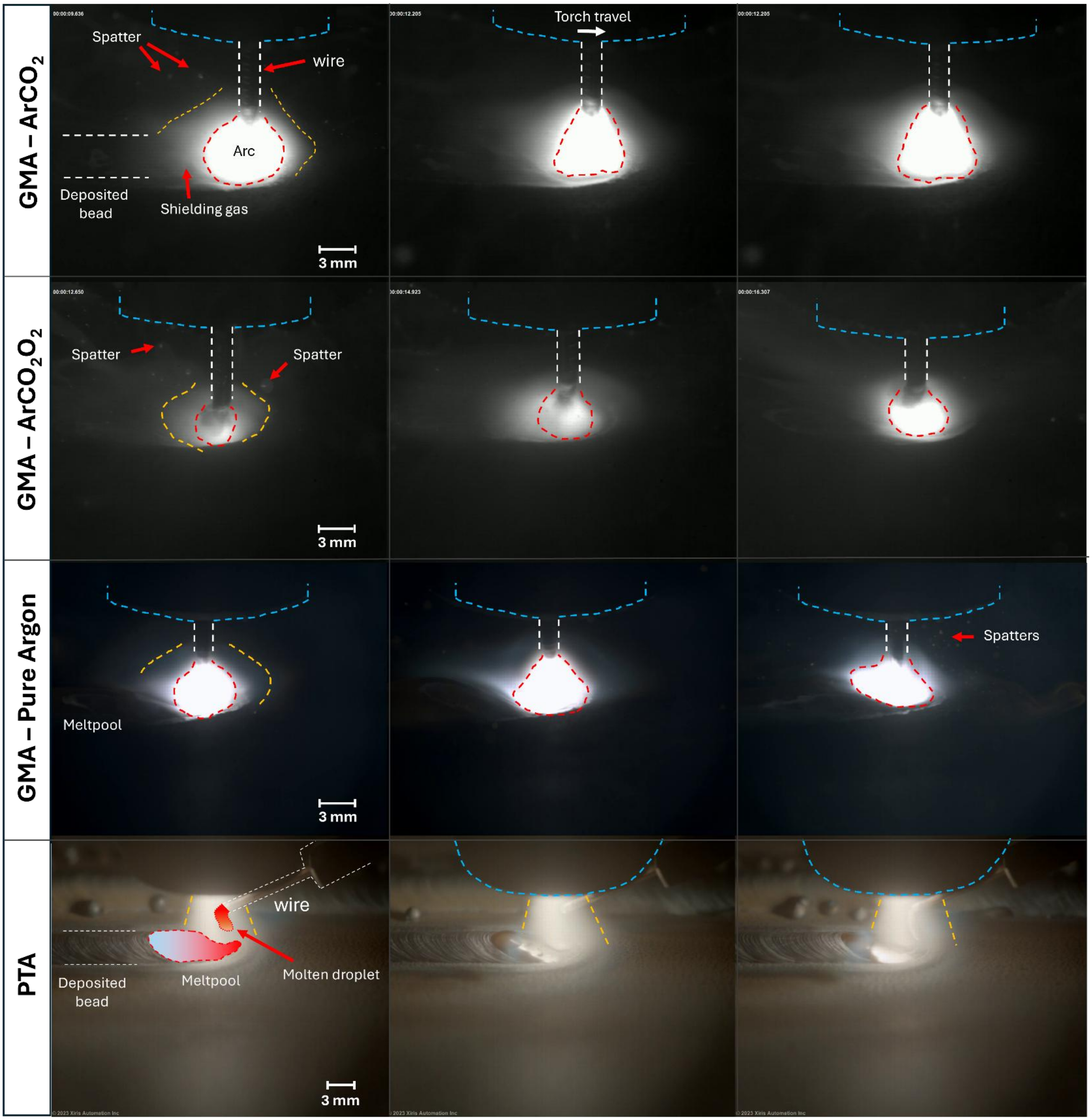

Fig. 6 Arc dynamics at different time instants under various shielding gases in GMA-based WAAM and under pure argon shielding in PTA-based WAAM using the cored-wire

The above results indicate that shielding gas in the WAAM process does more than protecting the molten metal; it significantly affects the arc stability, heat input, productivity, and the quality of the deposited material [47]. Therefore, selection of appropriate shielding gas is critical for optimal results in WAAM process. The behaviour of inert gases and gas mixtures using active gases is driven by their physical and chemical properties, especially at high temperatures. In WAAM, the centre of the arc can reach temperatures as high as 8000K and is influenced by the specific shielding gas used. Argon, an inert gas, is commonly chosen due to its low ionization energy, allowing for easier arc initiation. This is particularly beneficial for welding metals such as nickel, titanium, aluminium, and copper alloys [48]. Argon's low thermal conductivity results in lower heat input in the WAAM process. For these reasons, argon often serves as the primary component in gas mixtures, even when mixed with other gases.

In contrast, oxygen (O_2) and carbon dioxide (CO_2) are both oxidizing gases. Depending on the metal, gas mixtures are used to harvest their individual effects on the process. Hence, to achieve a stable arc in steel deposition, addition of oxidizing gases such as O_2 or CO_2 is common. CO_2, for instance, is inactive with metals at room temperature but becomes reactive at high temperatures, interacting with the molten metal alloys. Due to its higher thermal conductivity, CO_2 increases heat input, transforming the weld penetration profile from the narrow, finger-like shape (typical with pure argon) to a wider profile. Meanwhile, O_2 can form oxides at high temperatures, which is generally undesirable. However, in controlled amounts, O_2 enhances arc stability and wetting, leading to smoother bead surfaces.

For our study, we selected pure argon, $ArCO_2$, and $ArCO_2O_2$ gas mixtures to evaluate their respective influences on GMA-WAAM. We anticipated that using pure argon would produce lower heat input and a more concentrated, finger-like penetration profile due to its low thermal conductivity. Adding CO_2 and O_2 to the argon was expected to promote reactions with elements like silicon and manganese, forming a slag layer on the bead surface. This might also reduce these alloying elements in the weld, but the trade-off is improved arc stability by reducing arc wandering. Furthermore, the addition of CO_2 and O_2 should lead to a broader penetration profile, with O_2 specifically enhancing wetting and bead smoothness. The experimental results align with these predictions, showing variations in heat input, arc stability, and bead morphology based on the shielding gas composition.

3.2. Test specimens

To investigate the applicability of cored-wires (E90C-B3H4) for additive manufacturing with GMA and PTA-based WAAM processes, multilayer test walls were deposited with an alternating deposition strategy. For comparison, a standard solid wire (ER90S-B3) having the same chemical composition as cored-wire was also used to build the test walls. Seven walls deposited employing the two WAAM processes and wire types are shown in Fig. 7.

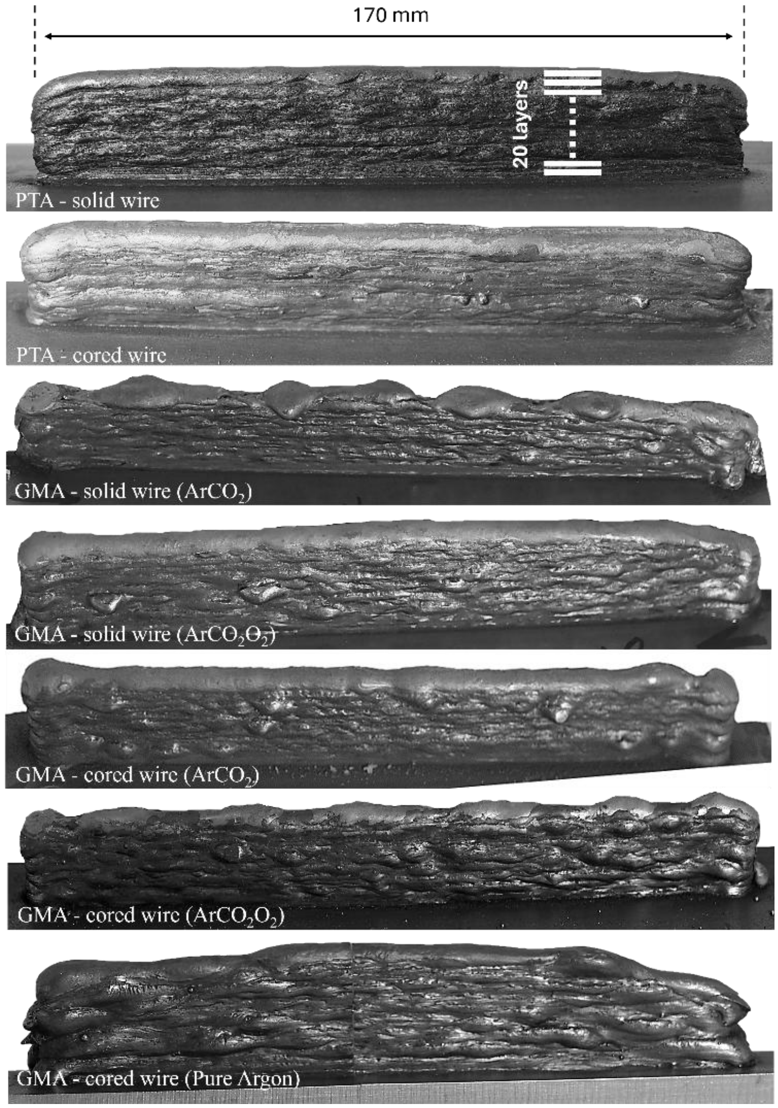

Fig. 7 Test walls deposited employing the cored and solid wires in GMA and plasma WAAM processes

The graph in Fig. 8 illustrates the heat variations across each wall layer using cored and solid wires in the two WAAM processes and the influence of shielding gases in the GMA-WAAM. The solid lines on the graph represent the results for solid wire, while the dashed lines show the results for cored-wire. Similarly, the shielding gases are colour-coded with black, red and blue for pure argon, $ArCO_2$ and $ArCO_2O_2$, respectively. The markers differentiate between the two processes: the squares denote the PTA while the circles show the results of GMA-WAAM. Several information can be obtained from this graph including the contribution of individual shielding gases in heat generation, the heat input across the two WAAM processes and most importantly the heat variations across the two wire types i.e. the cored-wire and the solid wire.

A key observation from the graph is the difference in heat input between cored-wire and solid wire. Cored-wire, characterized by its tubular shape and outer metal sheath filled with metal powders, typically produces a lower average heat input compared to solid wire. This is because the current flows only through the thin tubular section of the wire, increasing the current density and material deposition rate [38,49]. Under the same shielding gas and process parameters in GMA-WAAM, cored-wire resulted in substantially lower heat input. For instance, under $ArCO_2O_2$ and $ArCO_2$, solid wire produced average heat inputs of 665 J/mm and 690 J/mm, respectively, while cored-wire yielded 545 J/mm and 579 J/mm, reducing the average heat input by 16–18% compared to the solid wire.

Shielding gases also played a significant role in influencing the heat input in GMA process for a specific wire type. Pure argon, due to its inert nature and lower thermal conductivity compared to mixed gases, produced the lowest heat input with an average value of 467 J/mm for the test wall. The addition of CO_2 increases the ionization potential, resulting in higher arc temperature and average heat input. However, $ArCO_2O_2$ generated slightly lower heat input than $ArCO_2$, suggesting that oxygen addition could decrease heat input compared to $ArCO_2$ alone, yet still results in higher heat input than pure argon. These results further confirm those observed in bead-on-plate analysis.

Comparing the two WAAM processes, PTA generates a much higher heat input. The wire type does not influence the heat input significantly for the PTA-WAAM since the consumable wire is fed separately. The current does not flow through the externally fed wire but in the non-consumable tungsten electrode. Therefore, the cored-wire in case of PTA-WAAM does not affect the current density. However, GMA with cored-wire demonstrates lower heat input compared to solid wire under same conditions. The higher average heat input of solid wire across all shielding gases underscores its less efficient energy utilization compared to cored-wire.

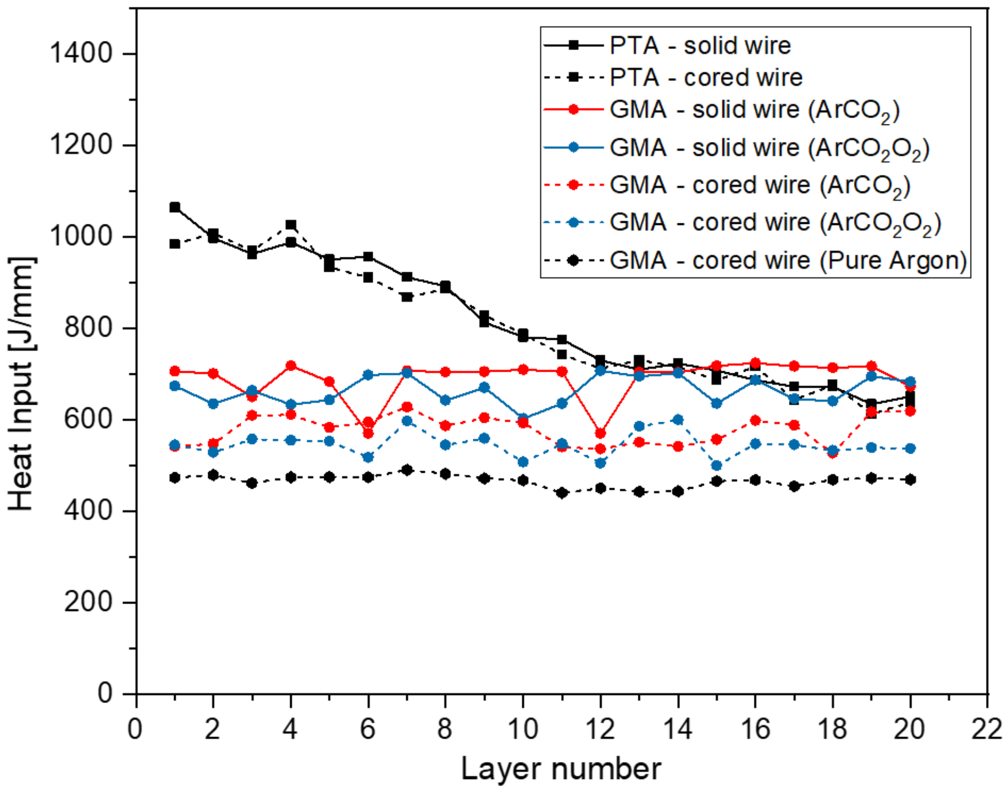

Fig. 8 Heat input variation across each layer for walls deposited with plasma and GMA WAAM using solid and cored-wire, employing various shielding gases for GMA-WAAM

To maintain the wall width from excessive growth in the building direction, current was gradually decreased in PTA-WAAM. For instance, as illustrated in Fig. 9, starting with an initial deposition current of 185 amperes and gradually reducing it to 125 amperes in the last two layers helped to regulate the heat input, thereby preventing the widening of the thin wall sections. A closer look reveals that solid wire is more susceptible to this strategy, where the wall deposited with solid wire formed a narrower cross-section compared to the cored-wire.

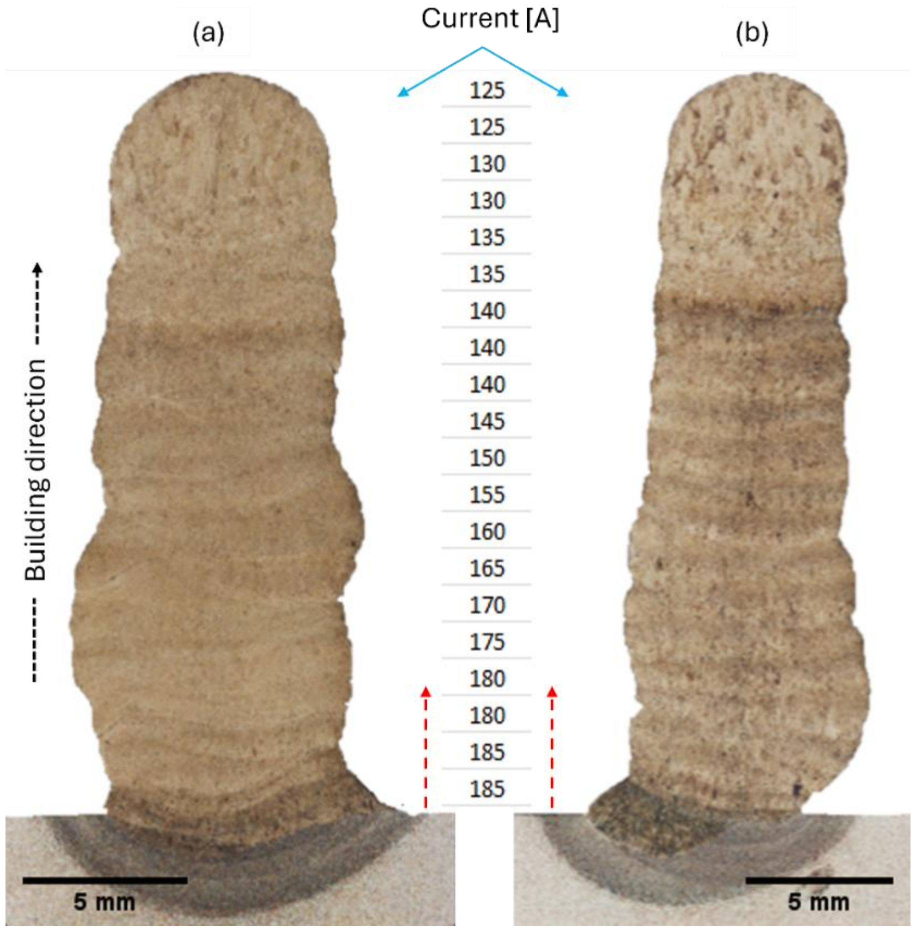

Fig. 9 Deposition strategy for thin walls in PTA-WAAM, employing (a) cored-wire, and (b) solid wire

3.2.1. Microstructural analysis

The microstructural studies were carried out at different locations of the test walls along the building direction (i.e. top, middle, and bottom zones) to study the variations in phases, grain structure and microstructural changes across the walls deposited with the cored and solid wires. Since both wires have similar chemical composition and contain chromium and molybdenum in appreciable quantities which promote the nucleation and growth of non-equilibrium hard phases, consequently helping to shift the continuous cooling transformation (CCT) curve to the right, making it easier to achieve a martensitic and bainitic microstructure [49]. Therefore, as shown in Fig. 10, the obtained microstructure is primarily consisted of a bainitic/martensitic structure for all specimens irrespective of the wire type. However, it is also composed of various microstructural phases and distinctive features randomly distributed along the building direction in the deposited walls based on the wire type and WAAM process.

A detailed comparison of the microstructures in cored vs solid wires for the test walls are reported in Fig. 11. The figure shows from left to right the microstructural features along the building direction at distinctive locations of the walls: bottom zone, middle zone, and upper zone for PTA-WAAM and under each shielding condition in GMA-WAAM, employing the solid and cored-wires respectively. For each microstructure shown, the WAAM process with shielding conditions are specified on the left while the corresponding wire type is indicated on the right to differentiate between them. In general, a fine microstructure is present at the bottom zone which tends to grow coarser in the middle section. The upper zone presents a finer microstructure while the heat affected zone (HAZ) is composed of a coarse polygonal structure. The microstructural differences across different regions on the walls result from thermal gradients and cooling rates during the WAAM process. The bottom zone in the proximity of substrate acts as a heat sink in the first few layers, leading to rapid cooling and fine microstructure. The higher cooling rates typically lead to shorter dendrite arm spacing and smaller cellular structures to result in finer structure. However, the middle zone experiences huge thermal shocks due to partial remelting of previously deposited layers, and further heat conduction from the upper layers through the middle section, reducing the cooling rate significantly. The corresponding slower cooling results in a coarser microstructure. The upper zone undergoes a faster cooling rate compared to the middle zone and dissipates the heat partly into the air and partly through conduction across the middle zone. This leads to a finer microstructure than the middle zone. Moreover, the layers deposited at the top section do not undergo significant remelting and help to maintain a faster cooling rate. Then the HAZ undergoes repeated thermal cycles with deposited layer; however, without the benefits of full remelting and re-solidification. Consequently, coarse polygonal structure results from grain growth as a result of consistent thermal exposure.

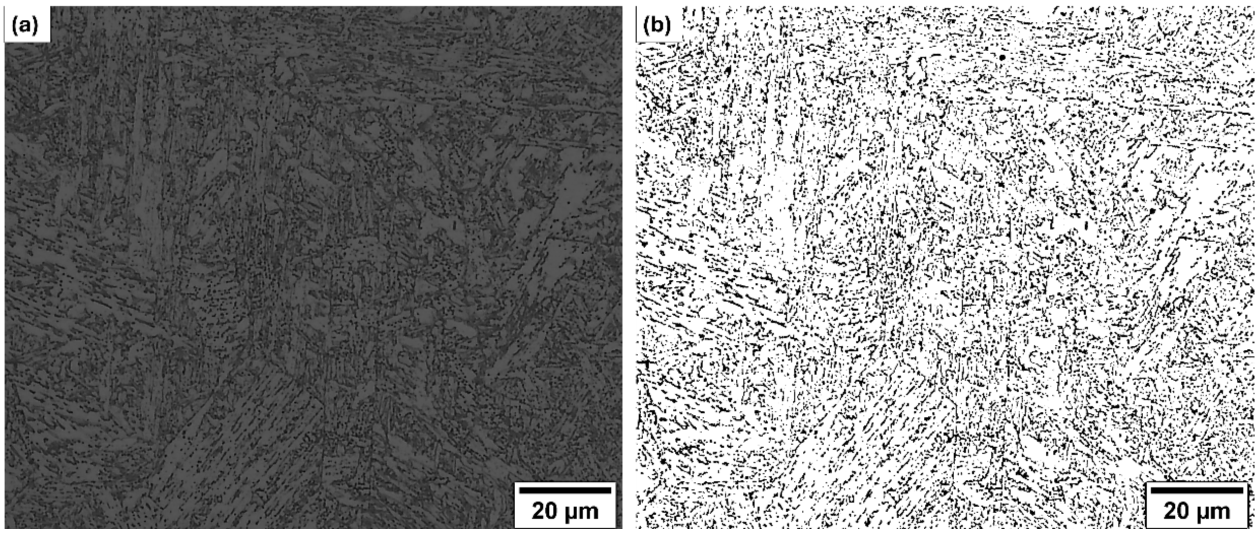

Fig. 10 Bainitic structure: (a) optical microscopic image (b) Showing lamellae distribution after image processing

However, the microstructure between the solid and cored wires shows a similar morphology for a certain process and shielding condition. Fig. 11(a – c) shows the microstructure of the wall deposited in PTA process using the solid wire. At the bottom of the wall, a transition from the re-melt area to HAZ is evident where a polygonal structure is dominant in the HAZ while a fine bainitic/martensitic structure is visible in the re-melt area. The middle section also exhibits a bainitic structure with short cementite lamellae, while in the top section the microstructure reveals prior austenite grain boundaries (PAGBs), which can be attributed to the slower cooling at the top section of the wall. In contrast, Fig. 11(d – f) presents the microstructure for the cored-wire from bottom to top in the PTA-WAAM, showing a fine bainitic/martensitic microstructure. Although the microstructure represents a similar morphology at the bottom compared to the solid wire, it tends to show coarser grains in the building direction. This shows the tendency of cored-wire to slightly form coarser grains in PTA process compared to the solid wire.

Under GMA with $ArCO_2$ shielding, Fig. 11(g – i) and Fig. 11(j – l) depict the microstructure for the solid versus cored wires, respectively, in the building direction. For the solid wire a very fine microstructure appears at the bottom zone that transitioned to a columnar structure in the middle zone. Further, the microstructure for the solid wire at the top zone changes to a fine needle-shaped microstructure. Comparing this microstructure of solid wire to that of the cored-wire, one can observe that they seem to exhibit an identical morphology under this shielding gas. In particular, a finer microstructure at the bottom, a coarse and partially columnar structure in the middle, while an acicular microstructure can be seen at the top section of the wall. Hence, the microstructure under the shielding of $ArCO_2$ in the GMA-WAAM seem to produce identical microstructure for the two wire types under study.

Similarly, Fig. 11(m – o) and Fig. 11(p – r) compare the microstructure of solid and cored wires, respectively, under the shielding of $ArCO_2O_2$. The microstructures of the solid and cored wires show a resemblance, especially in the bottom and top sections of the walls, where both exhibit a martensitic structure at the bottom region. The solid wire also features some banded colonies similar to pearlite colonies in the bottom and middle zones. Nevertheless, an identical coarse structure is evident in the middle zone for both wire types.

Finally, the microstructure of the wall deposited with cored-wire under the shielding of pure argon in GMA is shown in Fig. 11(s – u). A granular bainitic structure is seen at the bottom, followed by a columnar microstructure in the middle zone while an evident colonial structure is observed at the top section of the wall. Comparing this with the solid wire deposited in PTA process (given that same gas is used), significant differences can be observed in the microstructure. The microstructure of solid wire in the PTA process shows a more uniform structure in the building direction while the cored wire wall in GMA under pure argon exhibits more distinct layering and transition. However, these differences are attributed to various cooling dynamics and thermal histories across the two WAAM processes. It is important to mention that for a specific WAAM process and shielding gas, the two wires show identical microstructure across the walls. None of the walls show defects or impurities, hence showing the suitability of cored-wire in additive manufacturing.

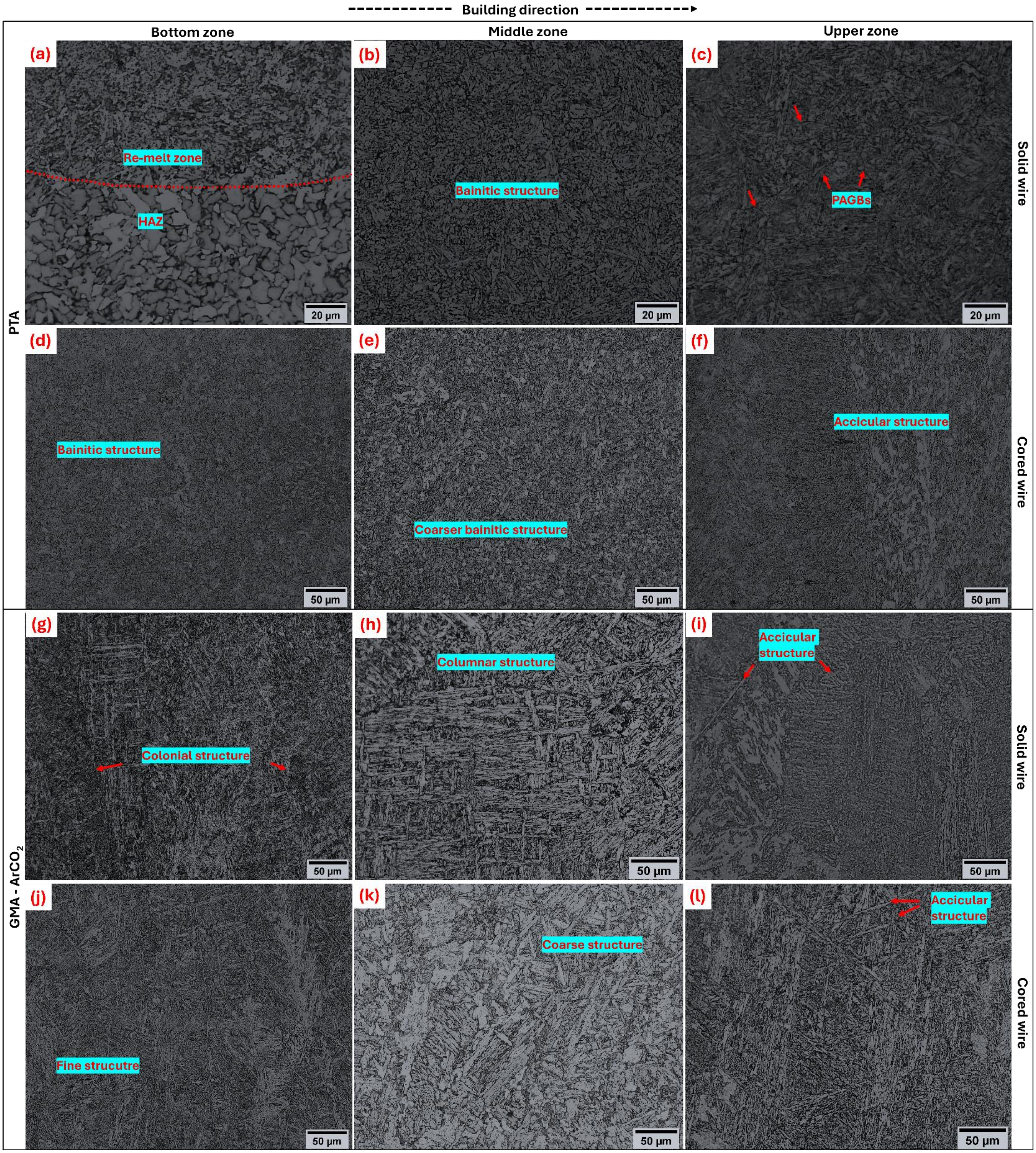
Building direction
Bottom zone
Middle zone
Upper zone
PTA
GMA - ArCO2
Solid wire
Cored wire
Solid wire
Cored wire
(a)
Re-melt zone
HAZ
20 µm
(b)
Bainitic structure
20 µm
(c)
PAGBs
20 µm
(d)
Bainitic structure
50 µm
(e)
Coarser bainitic structure
50 µm
(f)
Accicular structure
50 µm
(g)
Colonial structure
50 µm
(h)
Columnar structure
50 µm
(i)
Accicular structure
50 µm
(j)
Fine strucutre
50 µm
(k)
Coarse structure
50 µm
(l)
Accicular structure
50 µm

Continued...

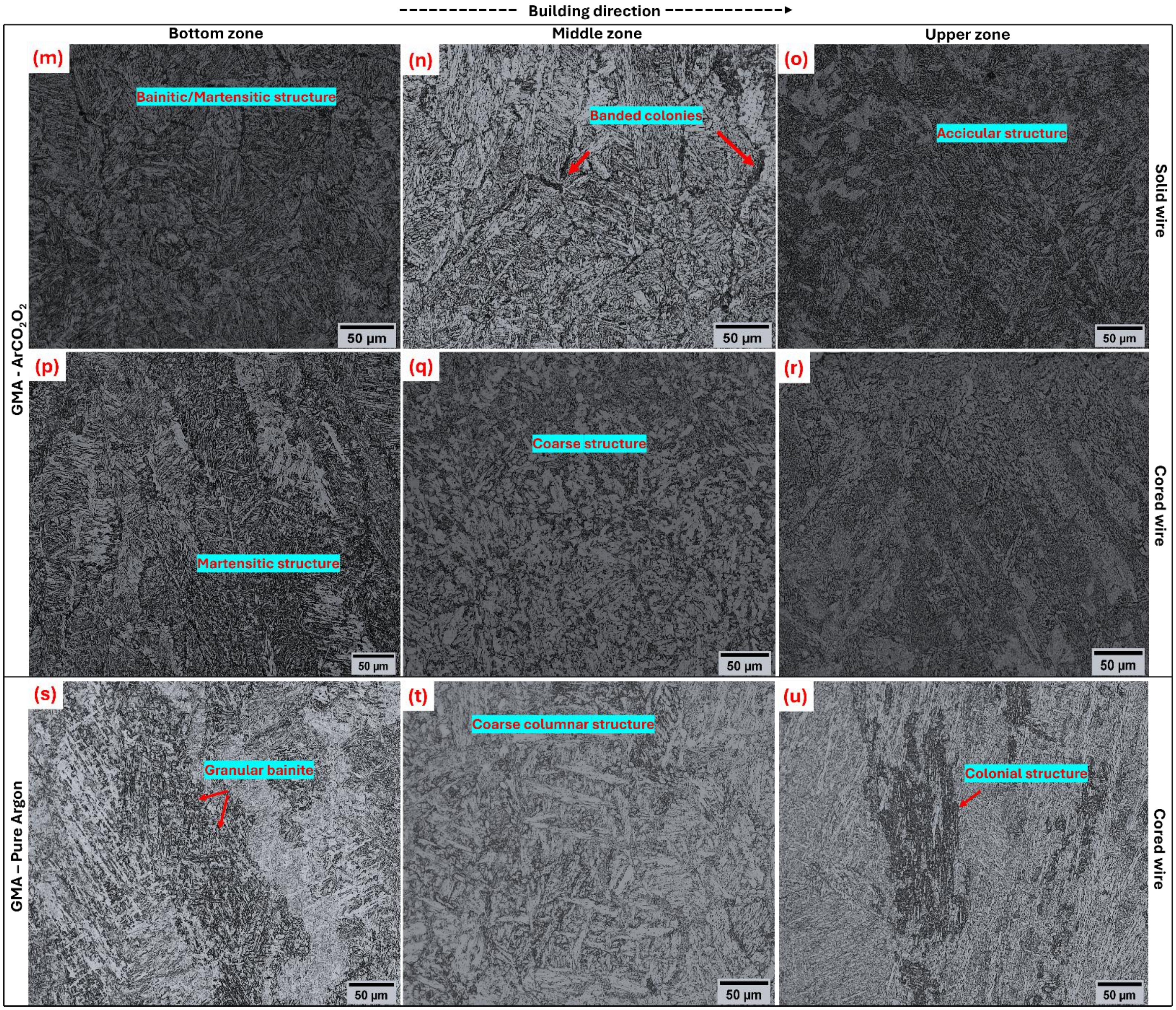

Fig. 11 Microstructural images of test walls deposited in the building direction, using solid and cored wires under GMA-WAAM (with various shielding gases) and PTA-WAAM, highlighting microstructural features and phase characteristics across the bottom, middle, and upper zones

The bainitic and martensitic structures observed within the GMA and PTA-deposited walls have implications for mechanical properties, demanding both strength and durability. Martensite is typically known for its high hardness and tensile strength. This microstructure would likely enhance wear resistance under low-stress conditions, as martensitic structures can withstand greater localized stress without undergoing significant deformation. However, martensitic structures may be more susceptible to brittleness, which could reduce toughness and impact resistance, particularly under cyclic or high impact loading conditions [50].

On the other hand, the bainitic structure observed in these walls can offer a favourable balance between hardness and toughness. Bainite's resilience to cyclic stress and its more ductile nature contributes to improved fatigue performance, which is beneficial in applications requiring sustained durability and resistance to both wear and mechanical impact [51]. Studies have shown that for bainitic and martensitic structures of the same steel, bainitic phases exhibit better wear resistance under high-stress abrasive conditions, whereas martensitic structures show better wear resistance in low-stress abrasive environments [50,52]. This suggests that the areas in our walls with bainitic structures would likely be suitable for high-wear applications and improved toughness while the martensitic phases promote yield strength and ultimate tensile strength.

The effect of chromium content, as also relevant to our material, is particularly notable in bainitic steels. Increased chromium enhances wear resistance, impact resistance, and fatigue properties, which are all desirable for durability in the WAAM process. The combination of these properties in bainitic structures aligns well with the performance requirements in applications such as those seen in automotive and railway industries [52,53] which traditionally use pearlitic structures with high carbon contents.

In the context of our study, the microstructural variations along the building direction in both the PTA and GMA walls can be expected to influence tensile strength, wear resistance, and impact toughness. The finer grains at the bottom zones typically correlate with higher tensile strength and wear resistance, while coarser grains in the middle zones might lower these properties but may enhance ductility and toughness to some extent. In summary, the observed microstructures can contribute to a balance of strength and wear resistance with adequate toughness and fatigue life that are important for high-performance applications of components produced by WAAM [54].

Supporting the results from optical microscopy, Fig. 12 represents the SEM images of the walls deposited in GMA and PTA processes under pure argon shielding, providing a clear representation of microstructural features in the building direction of the walls deposited using ER90S.

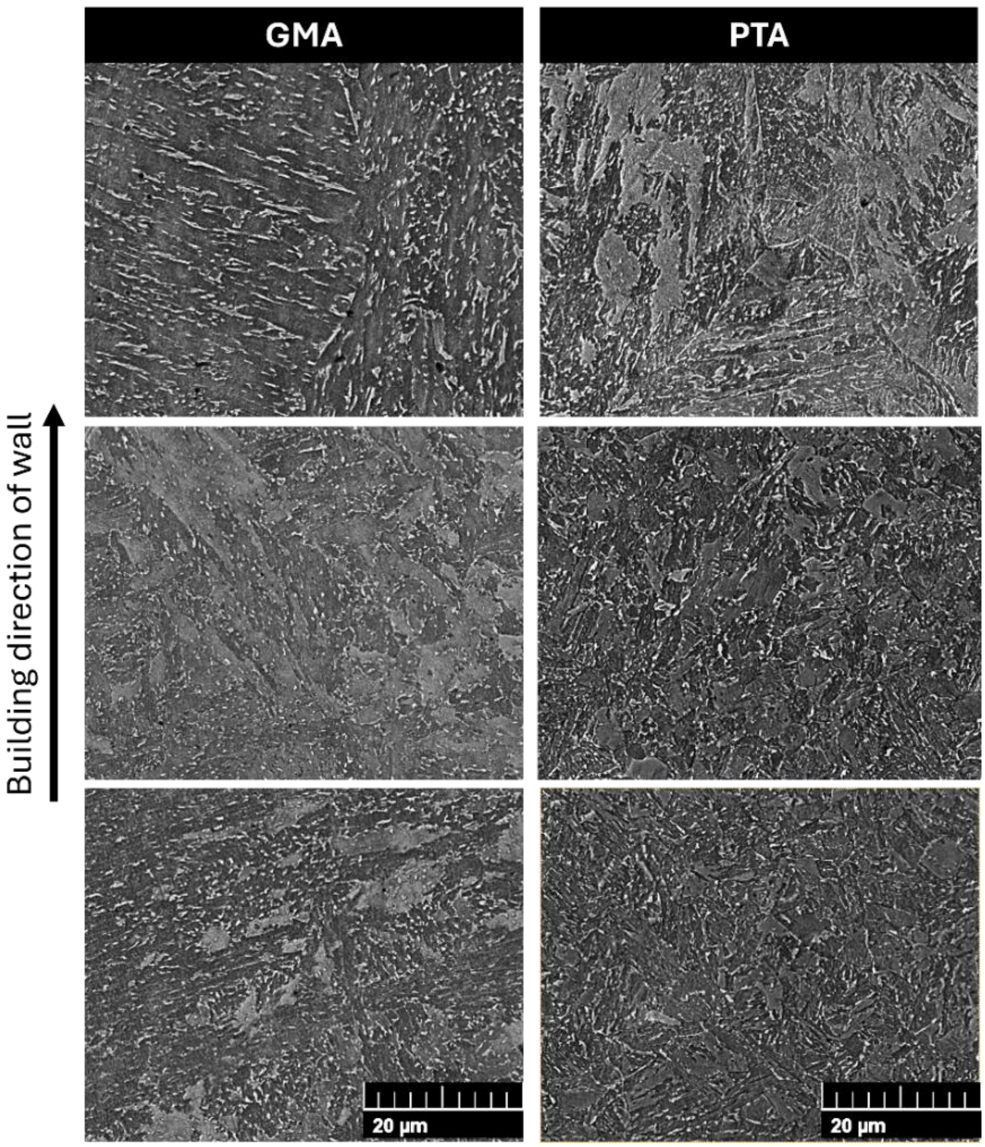

Fig. 12 SEM images in the building direction (i.e. top, middle and bottom sections) of the walls deposited in GMA and PTA processes under pure argon to provide a clear picture of microstructural features

GMA exhibits coarser columnar structures, particularly in the middle section, reflecting a slower cooling. In contrast, the PTA process shows a finer morphology with clear bainitic transformations, attributed to its localized and focused heat. The SEM images confirm that the PTA process produces a more refined and uniform microstructure along the building direction compared to GMA, aligning with the OM findings. These results demonstrate the superior microstructural control of PTA in achieving finer grains and uniformity.

In particular, the top and bottom sections of the wall from the GMA process exhibit a needle-shaped morphology, with a distinct columnar structure in the middle. In contrast, the PTA process reveals a finer acicular structure with bainitic transformations. The presence of prior austenite grain boundaries (PAGBs) at the top suggests thermal cycling, causing gradual heat accumulation and the formation of fine needle-like lathes.

3.2.2. Hardness

A detailed analysis of the microhardness was conducted to determine the hardness variations for the cored and solid wires across the walls deposited with GMA and PTA processes and the average hardness was calculated for each wall. Fig. 13(a) illustrates the hardness variations for the two wires in PTA-WAAM and in GMA-WAAM under the shielding of $ArCO_2O_2$ to give an overview of the hardness variations in the building direction across the walls. As shown on the graph, the 2.25Cr-1Mo possesses significantly higher hardness compared to the mild steel substrate. The main idea is to compare the hardness profiles for the cored and solid wires. Similarly, to further investigate the effects of shielding gases in GMA-WAAM and finally the hardness profiles across the GMA and PTA processes. Considering only one WAAM process at a time and comparing the hardness profiles of walls built with cored and solid wires, we can observe a slightly higher hardness trend across the walls deposited with solid wire. From the process point of view, PTA exhibits a higher hardness while the shielding gases also show different hardness profiles in the GMA-WAAM. Comparing the global hardness trend across the walls, we observe a slightly higher hardness at the bottom of the walls probably due to faster cooling in proximity with the cold substrate. The middle sections of the walls exhibit marginally lower hardness which then takes a sharp upward trend at the top sections. The corresponding hardness profiles align with the underlying microstructure observed in the preceding section.

Fig. 13(b) further concludes the hardness results for all the walls, showing the average hardness for the observed conditions. Three characteristic remarks could be followed from the obtained results based on the WAAM process, the wire type, and the shielding gases, respectively. From the process perspective, we can conclude that PTA-WAAM produced a slightly higher hardness compared to GMA-WAAM for the same wire type. Similarly, the solid wire yielded slightly higher hardness than the cored-wire. In addition, the shielding gases also effected the underlying hardness in the GMA process. For instance, the average hardness was slightly higher in the wall deposited under $ArCO_2$ shielding gas compared to $ArCO_2O_2$, when employing the solid wire. The same results can also be seen in the case of cored-wire where $ArCO_2$ and pure argon shielding gases yielded an average hardness of 266 HV compared to an average hardness of 245 HV for $ArCO_2O_2$ shielding, resulting in around 8% less hardness for the wall deposited under the shielding of $ArCO_2O_2$ gas.

In the comparison of solid vs cored wire in PTA-WAAM, the average hardness decreased by around 8.5% across the wall deposited with cored-wire. Notably, in GMA, using $ArCO_2$ shielding gas, the average hardness again showed 8.5% reduction with the cored-wire compared to solid wire. The reduction of average hardness across the cored-wire wall became more pronounced with the use of $ArCO_2O_2$ shielding gas, where cored-wire resulted in approximately 14.6% less hardness. However, the lowest hardness obtained from cored-wire, at 245 HV under $ArCO_2O_2$, still exceeds the AWS A5.28/A5.28M requirements of 95 – 97 Rockwell B (≈215 – 224 HV) for AWS ER90S-B3, confirming the suitability of the cored wire under study.

Further analysis revealed a reduction of around 4% in average hardness for GMA wall when employing the cored-wire under pure argon shielding. Similarly, when using the solid wire across the two processes, the same difference was observed under the shielding of pure argon in PTA process and $ArCO_2$ in GMA process. This could be because $ArCO_2$ contains 97.5% argon, leading to similar results across the two processes.

It is worth noting that all the walls exhibit a bainitic/martensitic microstructure, however, the walls deposited under GMA process demonstrate slightly lower hardness compared to those deposited via the PTA-WAAM. The PTA process has a more focused arc which results in smaller melt pools. The smaller melt pool solidifies more rapidly which usually results in smaller grain structure, as seen in walls deposited using the PTA-WAAM in the preceding section. Conversely, the GMA process has a larger arc column typically producing large melt pools, reducing the solidification rate, presumably resulting in slightly coarser microstructure. As per Hall-Petch mechanism, this can result in hardness reduction for walls deposited using the GMA process. However, approaching the middle and top sections of the walls, the heat accumulation seems to have a more pronounced effect due to the thermal history and corresponding slow cooling.

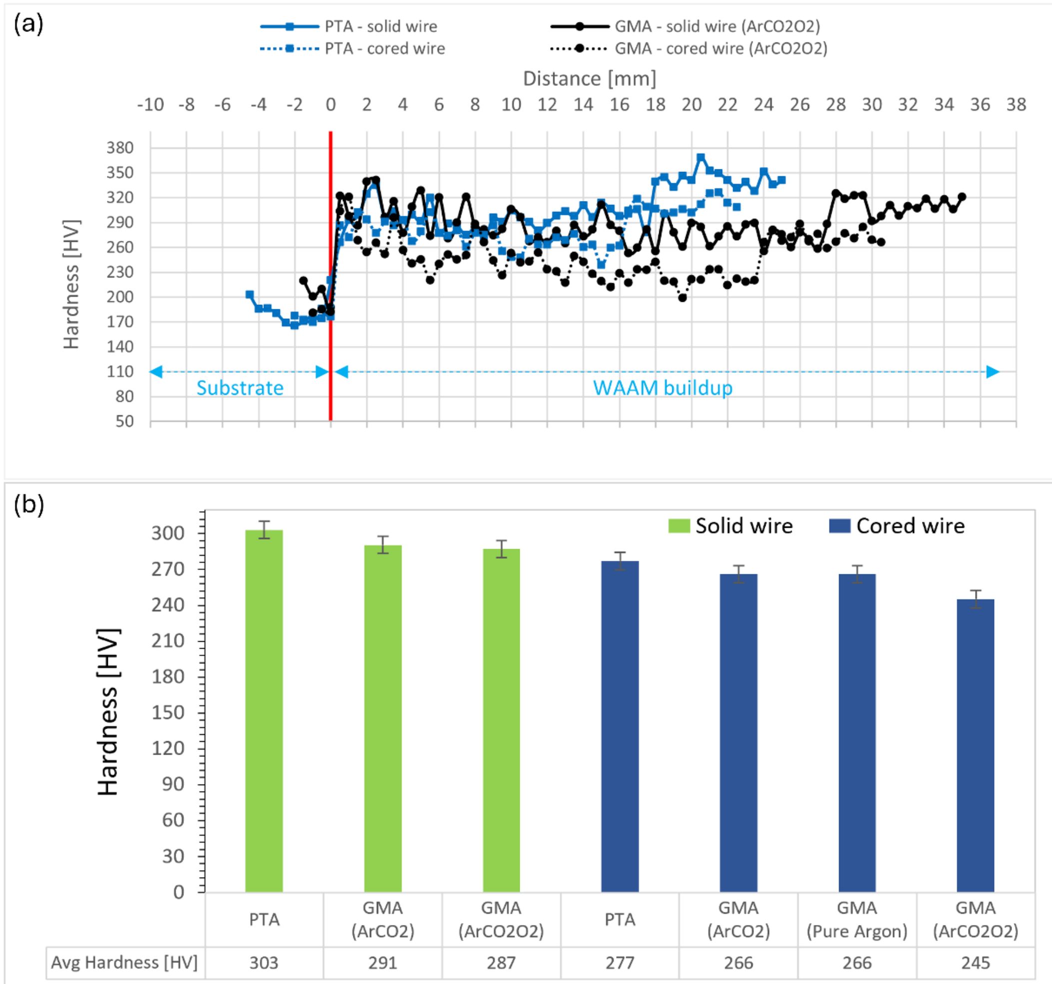

Fig. 13 Results for (a) Hardness profiles in PTA and GMA (under $ArCO_2O_2$ shielding) for cored and solid wires, (b) Average hardness of all the walls employing the two wires in the two WAAM processes

To provide a statistical validation of hardness results, a Tukey's method of pairwise comparisons at a 95% confidence level was conducted and the model was validated by analysis of variance, with a P-value < 5%. These results are summarised in Table 4. This approach provides a robust comparison of hardness results across the deposition processes, wire types, and shielding gas compositions. The interval plot in Fig. 14 graphically supports these results, showing the mean hardness values with 95% confidence intervals. Tukey's method groups (A – D) different factors based on their means and statistical significance. Means that do not share a letter are significantly different. The letter grouping is used to indicate which factors have similar means where Group A contains the highest means (PTA - Solid and GMA ($ArCO_2$) – Solid wire). Group B includes slightly lower means (GMA ($ArCO_2O_2$) – Solid wire and PTA – Cored wire). Finally, Group C contains GMA ($ArCO_2$) – Cored wire, and Group D includes the lowest mean (GMA ($ArCO_2O_2$) – Cored wire).

From a process perspective, PTA employing the solid wire achieved the highest hardness (Group A), demonstrating a statistically significant improvement over other combination. As seen from the microstructural analysis, this superior hardness can be attributed to the finer microstructure in the wall deposited with solid wire in PTA process. On the other hand, the wall deposited using cored wire in PTA exhibited a lower mean hardness, falling into Groups B and C, reiterating on the difference of wire type even within the same process. In GMA-WAAM, hardness values were generally lower, with the hardness of the wall deposited under GMA ($ArCO_2$) using the solid wire falling in Groups A and B, while wall deposited under GMA ($ArCO_2O_2$) using cored wire falls in Group D, showing the lowest mean hardness. These results emphasize that PTA-WAAM process, especially with solid wire, achieves higher mechanical performance in terms of hardness, likely due to a finer microstructure.

Table 4 Summary of the results from Tukey's method for Pairwise comparison of hardness from the two WAAM processes and shielding gas conditions deposited employing the solid and cored-wire

Tukey's method for Pairwise comparison at 95% confidence interval			
Process/Gases/Wire	Mean Hardness	Grouping	
PTA – Solid wire	303	A	
GMA (ArCO2) – Solid wire	291	A, B	
GMA (ArCO2O2) – Solid wire	287	B	
PTA – Cored wire	277	B, C	
GMA (ArCO2) – Cored wire	266	C	
GMA (ArCO2O2) – Cored wire	245	D	
Analysis of Variance			
Source	Degree of freedom	F-value	P-value
Factor	5	37.16	0.000
Error	428	-	-
Total	433	-	-

Solid wire generally produced higher hardness values than cored wire, a trend supported by the statistical groupings. For example, in PTA-WAAM, the mean hardness of solid wire deposits (303 HV) was higher than that of cored wire deposits (277 HV). Similarly, in GMA-WAAM with $ArCO_2$ shielding, solid wire deposits (291 HV) outperformed cored wire deposits (266 HV). The microstructural analysis in the previous section revealed similar features for a certain process and shielding gas type; however, it was found that solid wire tends to produce a slightly finer microstructure, especially at the bottom of each wall. Thus, the underlying statistical results correspond to those seen in previous discussions.

Shielding gas composition also played a critical role in the hardness values observed for GMA-WAAM deposits. The use of $ArCO_2$ shielding gas yielded higher hardness values for both solid (Groups A and B) and cored wires (Group C) compared to the more oxidizing $ArCO_2O_2$ mixture. Specifically, the wall deposited under GMA ($ArCO_2O_2$) using the cored wire showed the lowest hardness (Group D), indicating a significant reduction. This difference can be linked to the oxygen content in $ArCO_2O_2$, which may promote the formation of oxide inclusions and reduce weld pool quality, leading to softer microstructures. In contrast, the $ArCO_2$ shielding gas provides a more stable arc and effective shielding, supporting the formation of stronger microstructures.

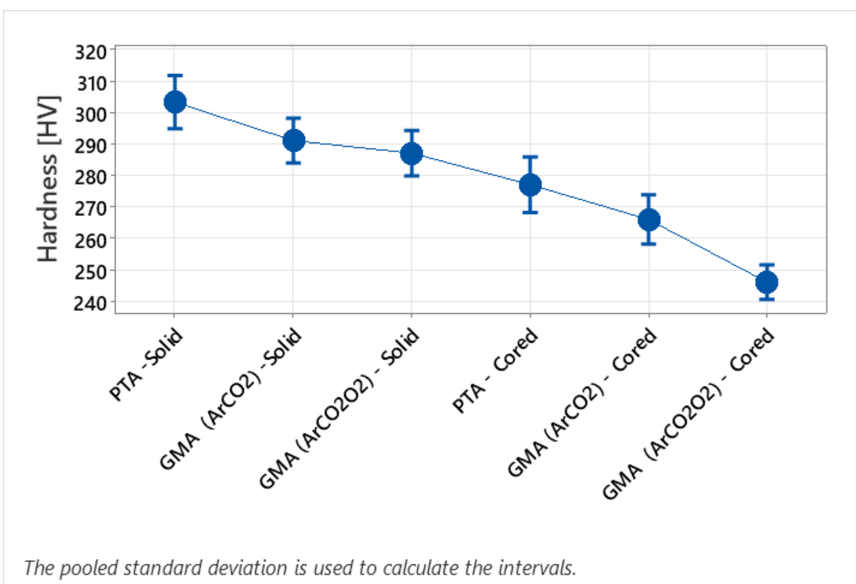

Fig. 14 Interval plot of hardness from Tukey's pairwise comparison

A thorough investigation of data revealed that a possible relationship exists between the average hardness of walls and the corresponding average heat input experienced across each wall. Fig. 15 demonstrates such a relationship, representing the average heat input trend with respect to average hardness for different walls in GMA-WAAM under various shielding gases and wire types. For example, under the shielding of $ArCO_2O_2$ using the solid wire, the average hardness of the wall slightly reduced when the heat input decreased compared to the wall deposited under $ArCO_2$ shielding. This was further verified in the case of cored-wire representing a comparable trend under similar conditions. These results are intriguing and suggest an interaction of a certain phenomenon specific to this alloy. In general, one can assume that a lower heat input could lead to faster cooling resulting in finer microstructure and higher hardness. However, this unique relationship for 2.25Cr-1Mo steel alloy, designed for high temperature applications, highlights the complexity of the relationship between heat input and hardness. The possible factors influencing this behavior could be alloy-specific, relating to thermal history or segregation. Higher heat input may promote the precipitation of specific carbides during the cooling process. The prolonged exposure at higher temperature facilitates the diffusion process more effectively. The high chromium and molybdenum contents stabilize martensite at higher temperatures. Similarly, higher heat input can cause segregation of chromium and molybdenum at grain boundaries, forming hard phases, hence increasing the hardness. Therefore, further investigations are suggested to unveil the underlying behavior in detail.

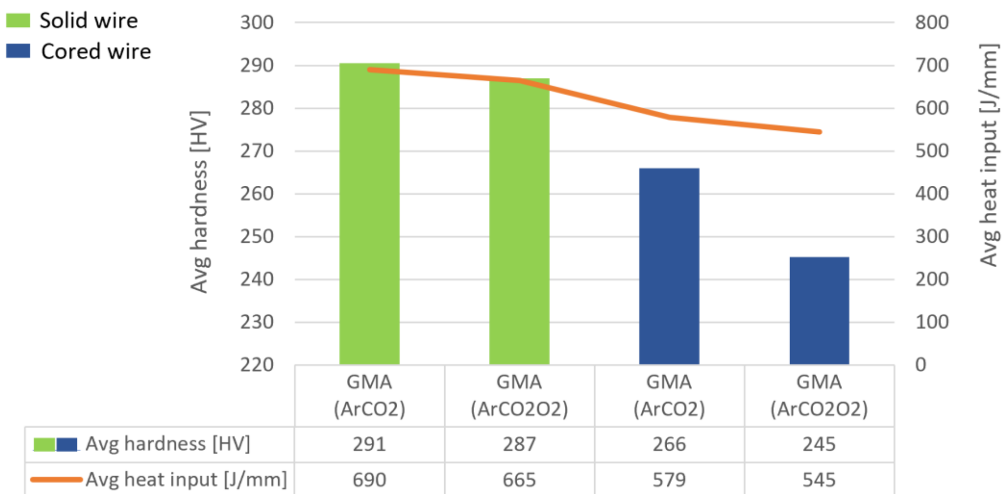

Fig. 15 Relationship between the average hardness and average process heat input

3.2.3. EDS analysis

Energy dispersive X-ray spectroscopy (EDS) elemental analysis was performed at arbitrary locations along the building direction of the thin walls deposited with solid and cored-wires and their compositions were averaged. Similarly, to compare the distribution of alloys and possible alloys' segregation, EDS maps were obtained from the center of the walls. Fig. 16(a) shows the site locations of elemental analysis and the positions of the EDS maps while Fig. 16(b) and Fig. 16(c) represent the results of average alloying elements on walls deposited with solid and cored-wires under PTA and GMA ($ArCO_2O_2$) processes, respectively. The elemental analysis shows that a small discrepancy exists among the alloying elements between the walls deposited under solid and cored-wires. However, these minor differences are not significant and correspond to the underlying ranges of elemental composition claimed by the wire suppliers. Moreover, comparing the walls deposited under these conditions between the two WAAM processes, we can conclude that a comparable range of these alloying elements exists. Nevertheless, if we strictly evaluate the two wire types, we can tell that very small differences of main alloying elements might have resulted in small variations of hardness. For example, the walls deposited under solid wire have slightly more chromium and molybdenum percentage compared to cored-wire, which could explain slightly higher hardness in Fig. 13(b).

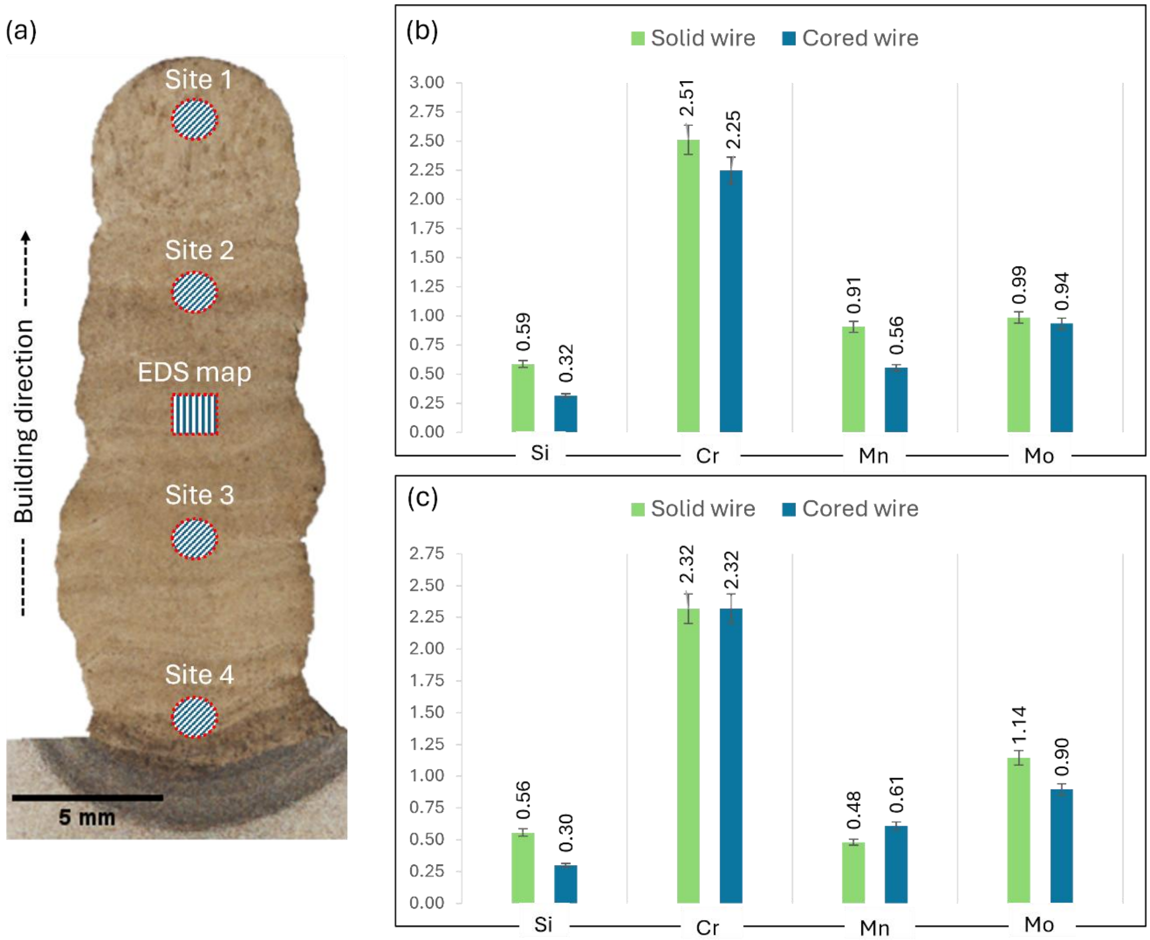

Fig. 16 EDS analysis: showing (a) site locations for EDS elemental analysis, and average composition of main alloying elements for walls deposited with solid and cored-wires for (b) PTA-WAAM and (c) GMA-WAAM under the shielding of ArCO2O2

The EDS maps of walls shown in Fig. 17 compare the elemental distribution of solid and cored-wire. The presented maps depict the elemental distribution of main alloying elements including Iron (Fe), Manganese (Mn), Chromium (Cr), Molybdenum (Mo) and Silicon (Si) in the center of the two walls deposited in PTA process. Iron being the primary constituent, uniformly distributed across the structures in both cases. Chromium and Molybdenum being the main alloying elements, responsible for high hardness and high-temperature stability during the service and hence they exhibit homogeneous distribution in the iron matrix for both the solid and cored-wires. Similarly, Manganese and Silicon are also evenly dispersed, indicating their consistent integration within the matrix. The absence of alloys' segregation and uniformity of elements for both wires indicate a homogeneous distribution of alloying elements which suggests that solid and cored-wire are equally effective in achieving a homogeneous composition for WAAM deposits. Therefore, the choice between the wire type might be influenced by other factors such as manufacturing preference, deposition rate, cost, specific application requirements and other factors. For instance, considering the manufacturing steps required for wire production, the application of cored-wire could be more cost-effective for manufacturing wires with custom compositions to incorporate desired properties compared to solid wires and meeting customized requirements of end users.

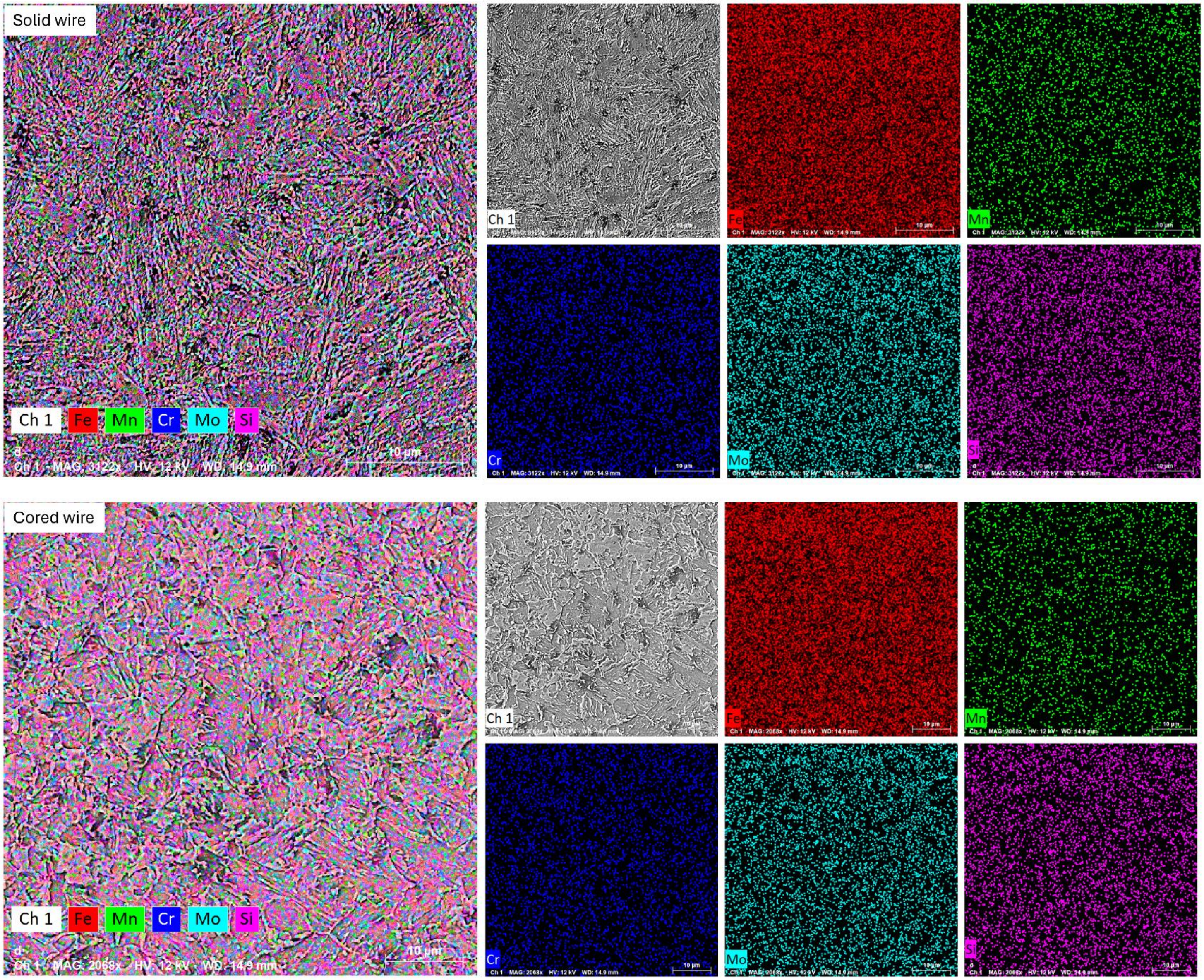

Fig. 17 Comparison of EDS maps of solid and cored-wires obtained at the center of the walls deposited under PTA-WAAM

Fig. 18 shows the EDS spectra for the standard solid wire and cored-wire obtained at the same locations as EDS maps, providing a detailed information about the elemental composition of each wire type. On the specified locations, the spectral peaks exhibit similar intensities for both wires, indicating a similar elemental composition, with iron being the primary element followed by chromium, molybdenum, manganese, and silicon. This uniformity further conforms to the previous results and suggests that the cored-wire is equally suitable in the layer-wise manufacturing with the benefits of tailored chemical composition and lower heat input.

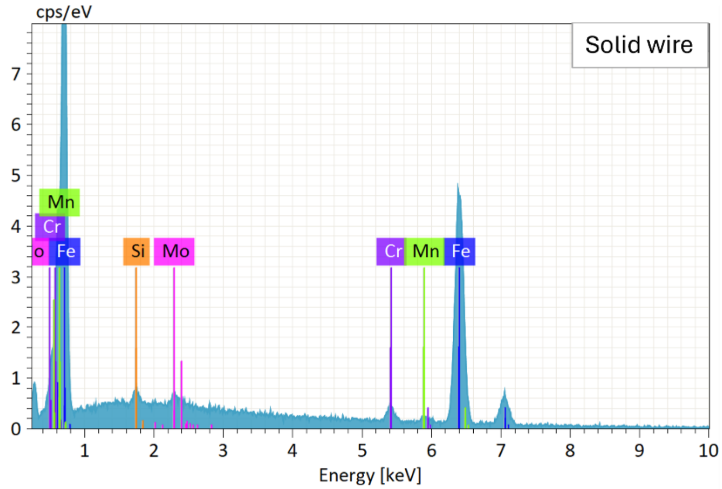

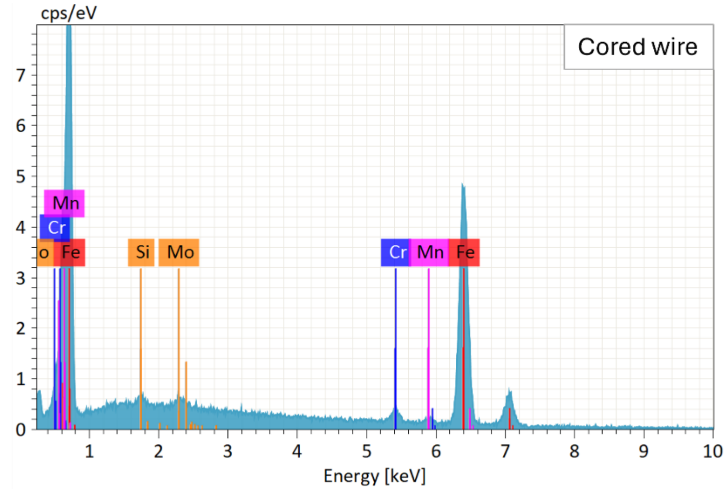

Fig. 18 EDS spectra comparison of solid and cored-wire

4. CONCLUSION

In this study two wires with same chemical composition but different forms were compared, metal cored-wire and solid wire. Two different WAAM processes were employed, the non-consumable electrode PTA and consumable electrode GMA with different shielding gases. The following points summarize the important results.

- PTA-WAAM produced a higher heat input compared to GMA-WAAM for similar deposition ratio. Similarly, the cored-wire led to a lower heat input than the solid wire in both WAAM processes, which is more evident in the case of GMA-WAAM. This could be attributed to the higher current density of the cored-wire.
- Under the same process parameters, shielding gases affected the heat input, arc dynamics and bead morphology in GMA-WAAM, with $ArCO_2$ and $ArCO_2O_2$ mixtures resulted in higher heat input and arc stability compared to pure argon.
- The microstructure primarily consisted of a bainitic/martensitic structure and for a specific process and shielding gas type the cored and solid wires exhibited identical microstructure.
- The hardness results showed a slightly higher hardness for solid wire; however, even the lowest hardness obtained with cored-wire exceeds the hardness requirements of AWS ER90S-B3 (95 – 97 Rockwell B ≈ 215 – 224 HV). From process point of view, PTA showed slightly higher hardness.
- Similarly, the EDS results showed comparable alloying elements and homogeneous maps for both cored and solid wires.
- The cored-wire resulted in similar chemical distribution and process response as solid wire. Therefore, proving to be a viable alternative of solid wire in WAAM process.

References

1. Svetlizky, D., Das, M., Zheng, B., Vyatskikh, A.L., Bose, S., Bandyopadhyay, A., Schoenung, J.M., Lavernia, E.J., Eliaz, N., 2021. Directed energy deposition (DED) additive manufacturing: Physical characteristics, defects, challenges and applications. Materials Today 49, 271–295. https://doi.org/10.1016/j.mattod.2021.03.020
2. Cunningham, C.R., Flynn, J.M., Shokrani, A., Dhokia, V., Newman, S.T., 2018. Invited review article: Strategies and processes for high quality wire arc additive manufacturing. Additive Manufacturing 22, 672–686. https://doi.org/10.1016/j.addma.2018.06.020
3. IvánTabernero, Paskual, A., Álvarez, P., Suárez, A., 2018. Study on Arc Welding Processes for High Deposition Rate Additive Manufacturing. Procedia CIRP 68, 358–362. https://doi.org/10.1016/j.procir.2017.12.095
4. Holliday, D.B., 1993. Gas-Metal Arc Welding, in: Olson, D.L., Siewert, T.A., Liu, S., Edwards, G.R. (Eds.), Welding, Brazing, and Soldering. ASM International, pp. 180–185. https://doi.org/10.31399/asm.hb.v06.a0001354
5. Key, J.F., 1993. Arc Physics of Gas-Tungsten Arc Welding, in: Olson, D.L., Siewert, T.A., Liu, S., Edwards, G.R. (Eds.), Welding, Brazing, and Soldering. ASM International, pp. 30–35. https://doi.org/10.31399/asm.hb.v06.a0001336

6. Alberti, E.A., Bueno, B.M.P., D'Oliveira, A.S.C.M., 2016. Additive manufacturing using plasma transferred arc. Int J Adv Manuf Technol 83, 1861–1871. https://doi.org/10.1007/s00170-015-7697-7
7. Yildiz, A.S., Davut, K., Koc, B., Yilmaz, O., 2020. Wire arc additive manufacturing of high-strength low alloy steels: study of process parameters and their influence on the bead geometry and mechanical characteristics. Int J Adv Manuf Technol 108, 3391–3404. https://doi.org/10.1007/s00170-020-05482-9
8. Rodrigues, T.A., Duarte, V.R., Tomás, D., Avila, J.A., Escobar, J.D., Rossinyol, E., Schell, N., Santos, T.G., Oliveira, J.P., 2020. In-situ strengthening of a high strength low alloy steel during Wire and Arc Additive Manufacturing (WAAM). Additive Manufacturing 34, 101200. https://doi.org/10.1016/j.addma.2020.101200
9. Çam, G., 2022. Prospects of producing aluminum parts by wire arc additive manufacturing (WAAM). Materials Today: Proceedings 62, 77–85. https://doi.org/10.1016/j.matpr.2022.02.137
10. Gierth, M., Henckell, P., Ali, Y., Scholl, J., Bergmann, J.P., 2020. Wire Arc Additive Manufacturing (WAAM) of Aluminum Alloy AlMg5Mn with Energy-Reduced Gas Metal Arc Welding (GMAW). Materials 13, 2671. https://doi.org/10.3390/ma13122671
11. Su, C., Chen, X., Gao, C., Wang, Y., 2019. Effect of heat input on microstructure and mechanical properties of Al-Mg alloys fabricated by WAAM. Applied Surface Science 486, 431–440. https://doi.org/10.1016/j.apsusc.2019.04.255
12. Davis, A.E., Breheny, C.I., Fellowes, J., Nwankpa, U., Martina, F., Ding, J., Machry, T., Prangnell, P.B., 2019. Mechanical performance and microstructural characterisation of titanium alloy-alloy composites built by wire-arc additive manufacture. Materials Science and Engineering: A 765, 138289. https://doi.org/10.1016/j.msea.2019.138289
13. C.H. Ng., M.J. Bermingham., D. Kent., M.S. Dargusch., 2021. High stability and high strength β-titanium alloys for additive manufacturing. Material Science and Engineering: A 816, 141326. https://doi.org/10.1016/j.msea.2021.141326
14. Kennedy, J.R., Davis, A.E., Caballero, A.E., Williams, S., Pickering, E.J., Prangnell, P.B., 2021. The potential for grain refinement of Wire-Arc Additive Manufactured (WAAM) Ti-6Al-4V by ZrN and TiN inoculation. Additive Manufacturing 40, 101928. https://doi.org/10.1016/j.addma.2021.101928
15. Hassel, T., Carstensen, T., 2020. Properties and anisotropy behaviour of a nickel base alloy material produced by robot-based wire and arc additive manufacturing. Weld World 64, 1921–1931. https://doi.org/10.1007/s40194-020-00971-7
16. Tanvir, A.N.M., Ahsan, Md.R.U., Ji, C., Hawkins, W., Bates, B., Kim, D.B., 2019. Heat treatment effects on Inconel 625 components fabricated by wire + arc additive manufacturing (WAAM) - part 1: microstructural characterization. Int J Adv Manuf Technol 103, 3785–3798. https://doi.org/10.1007/s00170-019-03828-6
17. Pant, H., Arora, A., Gopakumar, G.S., Chadha, U., Saeidi, A., Patterson, A.E., 2023. Applications of wire arc additive manufacturing (WAAM) for aerospace component manufacturing. Int J Adv Manuf Technol 127, 4995–5011. https://doi.org/10.1007/s00170-023-11623-7
18. Omiyale, B.O., Olugbade, T.O., Abioye, T.E., Farayibi, P.K., 2022. Wire arc additive manufacturing of aluminium alloys for aerospace and automotive applications: A review. Materials Science and Technology 38, 391–408. https://doi.org/10.1080/02670836.2022.2045549
19. Laghi, V., Gasparini, G., 2023. Explorations of efficient design solutions for Wire-and-Arc Additive manufacturing in construction. Structures 56, 104883. https://doi.org/10.1016/j.istruc.2023.104883
20. Choi, D.-H., Ahn, B.-W., Yeon, Y.-M., Jung, S.-B., 2012. Microstructures and Mechanical Properties of Friction Stir Welded 2.25Cr–1Mo Steel. Mater. Trans. 53, 1022–1025. https://doi.org/10.2320/matertrans.MBW201103
21. Chaudhari, R., Parikh, N., Khanna, S., Vora, J., Patel, V., 2022. Effect of multi-walled structure on microstructure and mechanical properties of 1.25Cr-1.0Mo steel fabricated by GMAW-based WAAM using metal-cored-wire. Journal of Materials Research and Technology 21, 3386–3396. https://doi.org/10.1016/j.jmrt.2022.10.158
22. Das, S., Vora, J.J., Patel, V., Li, W., Andersson, J., Pimenov, D.Y., Giasin, K., Wojciechowski, S., 2021b. Experimental investigation on welding of 2.25 Cr-1.0 Mo steel with regulated metal deposition and GMAW technique incorporating metal-cored-wires. Journal of Materials Research and Technology 15, 1007–1016. https://doi.org/10.1016/j.jmrt.2021.08.081
23. Das, S., Vora, J., Patel, V., Andersson, J., Pimenov, D.Y., Giasin, K., 2021a. Elucidating the Effect of Step Cooling Heat Treatment on the Properties of 2.25 Cr–1.0 Mo Steel Welded with a Combination of GMAW Techniques Incorporating Metal-Cored-wires. Materials 14, 6033. https://doi.org/10.3390/ma14206033
24. Prajapati, P., Badheka, V.J., Mehta, K.P., 2018. Hybridization of filler wire in multi-pass gas metal arc welding of SA516 Gr70 carbon steel. Materials and Manufacturing Processes 33, 315–322. https://doi.org/10.1080/10426914.2016.1244847
25. Lin, Z., Goulas, C., Ya, W., Hermans, M.J.M., 2019. Microstructure and Mechanical Properties of Medium Carbon Steel Deposits Obtained via Wire and Arc Additive Manufacturing Using Metal-Cored-wire. Metals 9, 673. https://doi.org/10.3390/met9060673
26. Dinovitzer, M., Chen, X., Laliberte, J., Huang, X., Frei, H., 2019. Effect of wire and arc additive manufacturing (WAAM) process parameters on bead geometry and microstructure. Additive Manufacturing 26, 138–146. https://doi.org/10.1016/j.addma.2018.12.013
27. Bajić, D., Mrdak, M., Bajić, N., Veljić, D., Rakin, M., Radosavljević, Z., 2020. Development of Coated Electrodes with Solid Wire and Flux-Cored Alloyed Wire for Microalloyed Steel Welding. Materials 13, 2152. https://doi.org/10.3390/ma13092152

28. Shamsujjoha, M., Licavoli, J., Lin, B., Harma, E., Patterson, R., Timmermann, T., Groeneveld, M., McLeod, L., Sanders, P., 2021. Tailoring microstructure of wire arc additively manufactured C–Mn–Si steel with post process heat treatment. Materials Science and Engineering: A 825, 141921. https://doi.org/10.1016/j.msea.2021.141921
29. Pixner, F., Buzolin, R., Zelić, A., Riedlsperger, F., Orłowska, M., Warchomicka, F., Decherf, M., Lasnik, M., Enzinger, N., 2022. Tailoring the alloy composition for wire arc additive manufacturing utilizing metal-cored-wires in the cold metal transfer process. Materials & Design 215, 110453. https://doi.org/10.1016/j.matdes.2022.110453
30. Treutler, K., Lorenz, S., Hamje, J., Wesling, V., 2022. Wire and Arc Additive Manufacturing of a CoCrFeMoNiV Complex Concentrated Alloy Using Metal-Cored-wire—Process, Properties, and Wear Resistance. Applied Sciences 12, 6308. https://doi.org/10.3390/app12136308
31. Liang, X., Su, Y., Yang, T., Dai, Z., Wang, Y., Yong, X., 2024. Study on the wear resistance and mechanism of AlCrCuFe2NiTix high-entropy surfacing alloys. Journal of Alloys and Compounds 971, 172510. https://doi.org/10.1016/j.jallcom.2023.172510
32. Marefat, F., Kapil, A., Banaee, S.A., Van Rymenant, P., Sharma, A., 2023. Evaluating shielding gas-filler wire interaction in bi-metallic wire arc additive manufacturing (WAAM) of creep resistant steel-stainless steel for improved process stability and build quality. Journal of Manufacturing Processes 88, 110–124. https://doi.org/10.1016/j.jmapro.2023.01.046
33. Kim, J.-D., Kim, J.W., Cheon, J.Y., Kim, Y.-D., Ji, C., 2020. Effect of Shielding Gases on the Wire Arc Additive Manufacturability of 5 Cr – 4 Mo Tool Steel for Die Casting Mold Making. Korean J. Met. Mater. 58, 852–862. https://doi.org/10.3365/KJMM.2020.58.12.852
34. Da Silva, L.J., Scotti, F.M., Fernandes, D.B., Reis, R.P., Scotti, A., 2021. Effect of O2 content in argon-based shielding gas on arc wandering in WAAM of aluminum thin walls. CIRP Journal of Manufacturing Science and Technology 32, 338–345. https://doi.org/10.1016/j.cirpj.2021.01.018
35. Yang, G., Deng, F., Zhou, S., Wu, B., Qin, L., Zheng, J., 2022. Influence of shielding gas nitrogen content on the microstructure and mechanical properties of Cu-reinforced maraging steel fabricated by wire arc additive manufacturing. Materials Science and Engineering: A 832, 142463. https://doi.org/10.1016/j.msea.2021.142463
36. Akbarzadeh, E., Yurtışık, K., Hakan Gür, C., Saeid, T., Tavangar, R., 2024. Influence of Shielding Gas on the Microstructure and Mechanical Properties of Duplex Stainless Steel in Wire Arc Additive Manufacturing. Met. Mater. Int. https://doi.org/10.1007/s12540-023-01623-3
37. Gürol, U., Dilibal, S., Turgut, B., Koçak, M., 2022. Characterization of a low-alloy steel component produced with wire arc additive manufacturing process using metal-cored-wire. Materials Testing 64, 755–767. https://doi.org/10.1515/mt-2021-2155
38. Czupryński, A., 2020. Comparison of Properties of Hardfaced Layers Made by a Metal-Core-Covered Tubular Electrode with a Special Chemical Composition. Materials 13, 5445. https://doi.org/10.3390/ma13235445
39. Shahryari Fard, S., Frei, H., Huang, X., Yao, M., 2021. Coordinated Heat and Feed Printing Strategy for Wire and Arc Additive Manufacturing of Metal-Cored-wires. J. of Materi Eng and Perform 30, 8841–8850. https://doi.org/10.1007/s11665-021-06338-3
40. American Welding Society, 2018. Development of Nickel-Added, Iron-Based, Slag-Free, Self-Shielded Metal-Cored-wire. WJ 97, 263–272. https://doi.org/10.29391/2018.97.023
41. Trinh, N.Q., Tashiro, S., Suga, T., Kakizaki, T., Yamazaki, K., Morimoto, T., Shimizu, H., Lersvanichkool, A., Bui, H.V., Tanaka, M., 2022. Effect of Flux Ratio on Droplet Transfer Behavior in Metal-Cored Arc Welding. Metals 12, 1069. https://doi.org/10.3390/met12071069
42. Zhai, W., Wu, N., Zhou, W., 2022. Effect of Interpass Temperature on Wire Arc Additive Manufacturing Using High-Strength Metal-Cored-wire. Metals 12, 212. https://doi.org/10.3390/met12020212
43. Yamaguchi, M., Komata, R., Furumoto, T., Abe, S., Hosokawa, A., 2022. Influence of metal transfer behavior under Ar and CO2 shielding gases on geometry and surface roughness of single and multilayer structures in GMAW-based wire arc additive manufacturing of mild steel. Int J Adv Manuf Technol 119, 911–926. https://doi.org/10.1007/s00170-021-08231-8
44. Pépe, N, S Egerland, P A Colegrove, D Yapp, A Leonhartsberger, and A Scotti. 'Measuring the Process Efficiency of Controlled Gas Metal Arc Welding Processes'. *Science and Technology of Welding and Joining* 16, no. 5 (July 2011): 412–17. https://doi.org/10.1179/1362171810Y.0000000029.
45. Fuerschbach, P. W. *Melting efficiency in fusion welding*. No. SAND-91-1326C; CONF-911003-9. Sandia National Labs., Albuquerque, NM (United States), 1991.
46. Hu, Y., Shi, Y.-H., Shen, X.-Q., Wang, Z.-M., 2017. Microstructure, Pitting Corrosion Resistance and Impact Toughness of Duplex Stainless Steel Underwater Dry Hyperbaric Flux-Cored Arc Welds. Materials 10, 1443. https://doi.org/10.3390/ma10121443
47. Weman, Klas, and Gunnar Lindén. 'MIG Welding Guide', 2006.
48. Singh, Ramesh. *Arc Welding Processes Handbook*. Beverly Hoboken: Scrivener publishing Wiley, 2021.
49. Shehu, N.U., Impey, S., Ganguly, S., 2022. Corrosion behavior of wire plus arc additive manufacturing (WAAM) built high strength pipeline steels 14. https://doi.org/10.48419/IMIST.PRSM/rhazes-v14.31153

50. Wei, Zhirui, Wei Wang, Man Liu, Junyu Tian, and Guang Xu. ‘Comparison of Wear Performance of Bainitic and Martensitic Structure with Similar Fracture Toughness and Hardness at Different Wear Conditions’. *Wear* 512–513 (January 2023): 204512. https://doi.org/10.1016/j.wear.2022.204512.
51. Yao, Zishan, Man Liu, Haijiang Hu, Junyu Tian, and Guang Xu. ‘Microstructure and Wear Properties of a Bainite/Martensite Multi-Phase Wear Resistant Steel’. *ISIJ International* 61, no. 1 (15 January 2021): 434–41. https://doi.org/10.2355/isijinternational.ISIJINT-2020-327.
52. Miranda, R.S., A.B. Rezende, S.T. Fonseca, F.M. Fernandes, A. Sinatora, and P.R. Mei. ‘Fatigue and Wear Behavior of Pearlitic and Bainitic Microstructures with the Same Chemical Composition and Hardness Using Twin-Disc Tests’. *Wear* 494–495 (April 2022): 204253. https://doi.org/10.1016/j.wear.2022.204253.
53. Clayton, P., K.J. Sawley, P.J. Bolton, and G.M. Pell. ‘Wear Behavior of Bainitic Steels’. *Wear* 120, no. 2 (December 1987): 199–220. https://doi.org/10.1016/0043-1648(87)90067-6.
54. Dalcin, Rafael Luciano, Rodrigo Afonso Hatwig, Leonardo Fonseca Oliveira, and Juliana Zottis. ‘Surface Processing to Improve the Fatigue Strength of Bainitic Steels – An Overview’. *International Journal of Engineering*, n.d.

Author Contributions All authors contributed to the study conception. Hambal Iqbal involved in experiments, data analysis and initial draft preparation. Goncalo Pardal and Wojciech Suder supervised experimental activities and conceptualization. Alessandro Ascari, Alessandro Fortunato and Stewart Williams coordinated the research activities, arranged the study visit, provided with lab facilities and travel arrangements. Erica Liverani and Leonor Neto helped in SEM and microstructural analysis. All the authors conducted reviews and editing of initial draft.

Funding No funds were received during the preparation of this manuscript.

Acknowledgments The authors thank Welding Alloys UK for providing the cored-wire for this study. The authors also acknowledge the team of Welding and Additive Manufacturing Centre at Cranfield University for their technical assistance.

Declarations

Competing Interests The authors declare no competing interests.